Unraveling Pathways of Elevated Ozone Induced by the 2020 Lockdown in Europe by an Observationally Constrained Regional Model: Non-Linear Joint Inversion of NO_x and VOC Emissions using TROPOMI

Amir H. Souri[1*], Kelly Chance[1], Juseon Bak[2], Caroline R. Nowlan[1], Gonzalo González Abad[1], Yeonjin Jung[1], David C. Wong[3], Jingqiu Mao[4,5], and Xiong Liu[1]

[1]Atomic and Molecular Physics (AMP) Division, Harvard–Smithsonian Center for Astrophysics, Cambridge, MA, USA

[2]Institute of Environmental Studies, Pusan National University, Busan, South Korea

[3]U.S. Environmental Protection Agency, Center for Environmental Measurement & Modeling, Research Triangle Park, NC, USA

[4]Geophysical Institute, University of Alaska Fairbanks, Fairbanks, AK, USA

[5]Department of Chemistry and Biochemistry, University of Alaska Fairbanks, Fairbanks, AK, USA

* Corresponding author: ahsouri@cfa.harvard.edu

Abstract. Questions about how emissions are changing during the COVID-19 lockdown periods cannot be answered by observations of atmospheric trace gas concentrations alone, in part due to simultaneous changes in atmospheric transport, emissions, dynamics, photochemistry, and chemical feedback. A chemical transport model simulation benefiting from a multi-species inversion framework using well-characterized observations should differentiate those influences enabling to closely examine changes in emissions. Accordingly, we jointly constrain NO_x and VOC emissions using well-characterized TROPOMI HCHO and NO_2 columns during the months of March, April, and May 2020 (lockdown) and 2019 (baseline). We observe a noticeable decline in the magnitude of NO_x emissions in March 2020 (14-31%) in several major cities including Paris, London, Madrid, and Milan expanding further to Rome, Brussels, Frankfurt, Warsaw, Belgrade, Kyiv, and Moscow (34-51%) in April. However, NO_x emissions remain at somewhat similar values or even higher in some portions of the UK, Poland, and Moscow in March 2020 compared to the baseline possibly due to the timeline of restrictions. Comparisons against surface monitoring stations indicate that the constrained model underrepresents the reduction in surface NO_2. This underrepresentation correlates with the TROPOMI frequency impacted by cloudiness. During the month of April, when ample TROPOMI samples are present, the surface NO_2 reductions occurring in polluted areas are described fairly well by the model (model: -21±17%, observation: -29±21%). Changes in VOC emissions are dominated by eastern European biomass burning activities and biogenic isoprene emissions. Results support an increase in surface ozone during the lockdown. In April, the constrained model features a reasonable agreement with maximum daily 8 h average (MDA8) ozone changes observed at the surface (*r*=0.43), specifically over central Europe where ozone enhancements prevail (model: +3.73±3.94%, +1.79 ppbv, observation: +7.35±11.27%, +3.76 ppbv). The model suggests that physical processes (dry deposition, advection, and diffusion) decrease MDA8 surface ozone in the same month on average by -4.83 ppbv, while ozone production rates dampened by largely negative $J_{NO2}[NO_2]-k_{NO+O3}[NO][O_3]$ become less negative, leading ozone to increase by +5.89 ppbv. Experiments involving fixed anthropogenic emissions suggest that meteorology contributes to 42% enhancement in MDA8 surface ozone over the same region with the remaining part (58%) coming from changes in anthropogenic emissions. Results illustrate the capability of satellite data of major ozone precursors to help atmospheric models capture ozone changes induced by abrupt emission anomalies.

1. Introduction

Continuous monitoring of air pollution by satellites can help our understanding of both anthropogenic and biogenic variability and change caused by rapid economic recession [Castellanos and Boersma, 2012] and regulations [Krotkov et al., 2016; Souri et al., 2020a]. Earth's atmosphere has substantially become more polluted since the industrial era in comparison to its original environmental condition [Li and Lin, 2015], thus any abrupt hiatus in anthropogenic (man-made) emissions should result in an immediate impact on relatively short lifetime pollutants such as nitrogen dioxide (NO_2), formaldehyde (HCHO), and tropospheric ozone (O_3). The beginning of the global COVID-19 pandemic in early 2020 [Fauci et al., 2020] provided such an abrupt change in human activities [Le Quéré et al., 2020]. A first step to fully understand how much of these impacts are related to the pandemic lockdowns is to disentangle the physical and chemical processes determining their ambient concentrations. Unraveling those processes require precise, continuous observations of physical and chemical states and emission rates, which are not routinely available on global, continental and regional scales. Therefore, we resort to using a model realization attempting to reproduce such an intricate system. Models without observational guidance are incapable of numerically representing the real world [Lorenz, 1963], so our best option to improve a model is to constrain some of its prognostic inputs using well-characterized observations. Accordingly, the framework of this study is centered around inverse modeling and data assimilation.

Significant attention has been given to documenting the lockdown-related changes in atmospheric composition around the world using both in-situ and satellite observations [e.g., Sicard et al., 2020; Shi and Brasseur, 2020; Lee et al., 2020; Salma et al., 2020; Le Quéré et al., 2020; He et al., 2020; Le et al., 2020; Miyazaki et al., 2020; Liu et al., 2020; Barré et al., 2020; Goldberg et al., 2020; Ordóñez et al., 2020; Wyche et al., 2021; Bekbulat et al., 2020; Gaubert et al., 2021]. The broad picture is consistent among these studies; the lockdown drastically reduced the concentrations of NO_x, CO, and SO_2 and some types of particulate matter, whereas the concentrations of several secondarily formed compounds such as ozone behaved in non-linear ways due to emissions and/or meteorology. To the best of our knowledge, changes in volatile organic compounds (VOCs) over Europe have not been reported.

The motivations of this study are to determine the capability of a regional model constrained by satellite HCHO and NO_2 columns to capture near-surface pollution, and if local ozone production rates are the driving factors for heightening ozone pollution during the 2020 lockdown. In other words, what chemical and physical processes are associated with the elevated ozone? How representative are satellite observations at capturing surface air quality through an inversion context? Is meteorology the primary factor in shaping elevated ozone as suggested by Ordóñez et al. [2020]?

To address these pivotal questions, it is desirable to constrain models using multi-species observations because relationships between the atmospheric compounds such as HCHO and NO_2 are importantly intertwined [Marais et al., 2012; Valin et al., 2016; Wolfe et al., 2016; Souri et al., 2020a,b]. Accordingly we build our inversion framework upon a non-linear joint analytical inversion of NO_x and VOCs proposed in Souri et al. [2020a] using TROPOMI HCHO and NO_2 observations in Europe. Performing this type of inversion not only enables us to precisely quantify the impact of the pandemic on emissions (along with its uncertainty, as the inversion framework is analytical) but also paves the way for estimating the resulting changes on different pathways of surface ozone.

2. Measurements, Modeling, and Methods

2.1. Satellite Observations

2.1.1. TROPOMI NO_2

We use daily offline S5P TROPOMI tropospheric NO_2 slant columns [Copernicus Sentinel data processed by ESA and Koninklijk Nederlands Meteorologisch Instituut (KNMI), 2019] derived from a two-step framework involving DOAS spectral fitting in conjunction with a stratosphere/troposphere decoupler [Boersma et al., 2018]. The time periods of this study are March, April, and May 2020 and 2019. The data provide Jacobians of light intensity with respect to optical thickness (i.e., vertically-resolved scattering weights) which are dependent on scene surface reflectivity, the cloudiness of the assumed Lambertian clouds, and sensor viewing geometry.

Aerosol effects on the scattering weights are not taken into consideration. Based on radiative transfer calculations and satellite-based aerosol products, Jung Y. et al [2019] and Cooper et al. [2019] observed small changes (<10%) in AMFs with and without considering the aerosol impacts in Europe in springtime. This tendency likely results from a low aerosol optical depth.

The 2019 TROPOMI observations used in this study have a spatial resolution of 7×3.5 km^2, whereas those in 2020 have a spatial resolution of 5.5×3.5 km^2. The NO_2 products for the study time period were produced by processor versions v01.02.02 (1 March 2019 – 20 March 2019) and v01.03.02 (20 March 2019 onward). The v01.03.02 processor includes an update to the FRESCO-S cloud algorithm and improvements to a quality flag variable. NO_2 validation from processors v01.02.02 and v01.03.02 shows similar biases and dispersion [Lambert et al., 2020], as do comparisons from before and after the pixel spatial resolution change [Verhoelst et al., 2021]. We extract good quality pixels based on the main quality flag (qa_flag) > 0.75, which removes retrievals flagged as bad and pixels over snow/ice or with cloud radiance fractions > 0.5, and resample them to our 15-km regional model (discussed later) using bilinear interpolation. Since vertical column densities (VCDs) depend on assumed gas profile shape (i.e., they are quasi-observations), we recalculate those shape factors using profiles from our constrained chemical transport model. Shape factors are re-estimated by calculating the ratio of the vertical column of total air to the simulated vertical column of NO_2

multiplied by the mixing ratios of NO_2 profile from the regional model [Martin et al., 2002].

Satellite remote sensing observations are usually far more stable than they are accurate. This can make the data practical for measuring relative changes in emissions, but may necessitate the use of a bias correction for absolute emissions estimates. Moreover, the systematic and random errors associated with satellite retrievals may differ markedly from location to location. It is therefore crucial to thoroughly validate columns against independent observations. To this end, we compile statistics reported in several validation studies focusing on the TROPOMI tropospheric NO_2 product and summarize their findings in Table 1. The most comprehensive global study to date is a comparison of TROPOMI tropospheric NO_2 with that derived from 19 MAX-DOAS instruments [Verhoelst et al., 2021]. This study indicates there is a low bias in TROPOMI tropospheric NO_2 of -23 to -37% relative to MAX-DOAS at clean to moderately polluted sites, and as large as -51% at highly polluted sites. When considering all sites, the overall median bias in this study was found to be -37%, with a dispersion of 3.5×10^{15} molec/cm^2 (defined as half of the 68% interpercentile). No obvious seasonal patterns were found in the biases. These results are consistent with other validation studies which have observed a low bias in TROPOMI tropospheric NO_2 [Chan et al., 2020; Griffin et al., 2019; Judd et al., 2020]. A potential significant source of bias in polluted regions is the relatively low spatial resolution ($1\times1^\circ$) TM5-MP prior profiles used in the TROPOMI air mass factor calculation. Several validation studies have shown the low bias in TROPOMI NO_2 can be reduced in polluted regions by 5-17% through the use of higher spatial resolution model a priori profiles or other improvements in the AMF calculation [Chan et al., 2020; Griffin et al., 2019; Judd et al., 2020; Zhao et al., 2020].

Directly incorporating these numbers into an inversion model is challenging, mainly because of spatiotemporal variability in the satellite errors. Ideally, the relationship between errors and retrieval inputs (e.g., albedo, scene radiance, profiles, etc.) would be used as an additional cost function in the inversion, commonly known as variational bias correction [e.g., Auligné et al., 2007]. In the absence of such relationships, we use the biases reported in the validation studies.

In the case of NO_2, we uniformly scale up the satellite tropospheric columns by 25%. This bias estimate is derived by first assuming a 37% low bias in the columns over polluted regions as reported by Verhoelst et al. [2021]. In turn, this low bias can be mitigated somewhat by the application of high spatial resolution profiles in the air mass factor calculation, such as the ones used in this study. Table 1 summarizes the results from several TROPOMI validation studies at specific locations that calculated NO_2 using model profiles with higher spatial resolution than the operational TROPOMI ($1^{o}\times1^{o}$) profiles (see Table 1 columns "Modification" and "Modified Bias"). In these studies, modified columns show increases ranging from 0 - 25%. Based on these results, we assume a low bias of 37% can be mitigated by ~12% through the use of high spatial resolution profiles, for a resulting total low bias of 25%. This bias is likely not valid over pristine areas, where validation studies show lower biases in TROPOMI NO_2 [Verhoelst et al., 2021, Wang et al., 2020, Zhao et al., 2020]; nonetheless, we previously observed in Souri et al. [2020a] that the low signal-to-noise ratios of those column amounts resulted in small changes in the top-down emissions. We assume the errors of observations originate from two main sources: i) the precision error provided with the data ($e_{precision}$) and ii) a fixed error estimated from comparisons to in-situ measurements (e_{const}). Mathematically, the final error is:

$$e_O^2 = e_{const}^2 + \frac{1}{n^2}\sum_{i=1}^{n} e_{precision,i}^2 \qquad (1)$$

where n is the number of samples for a given grid and e_{const} equals to 1.1×10^{15} molec/cm^2 ($<6\times10^{15}$ molec/cm^2) in clean regions and 3.5×10^{15} molec/cm^2 ($>=6\times10^{15}$ molec/cm^2) in moderately to highly polluted regions. These regions are defined based on the wide ranges reported in Verhoelst et al. [2021] ($3-14\times10^{15}$ molec/cm^2 for moderately to highly polluted regions).

2.1.2. TROPOMI HCHO

We use daily offline S5P TROPOMI HCHO total slant columns [Copernicus Sentinel data processed by ESA, German Aerospace Center (DLR), 2019]. A full description of the algorithm can be found in De Smedt et al. [2018]. The HCHO products for the study time period were produced by processor versions v01.01.05 (1 March 2019 – 28 March 2019), v01.01.06 (28 March 2019 – 23 April 2019) and v01.01.07 (23 April 2019 onward). The newer versions have added updates to the surface classification climatology and cloud products that might have some effects on the magnitude of HCHO in cloudy scenes. We again remove bad pixels based on qa_flag < 0.75 and recalculate shape factors using the simulated profiles derived from our regional model.

Validation efforts reported in the sixth Quarterly Validation Report of the Copernicus Sentinel-5 Precursor Operational Data Products [Lambert et al., 2020] indicate varying biases depending on the magnitude of HCHO concentrations in comparison to ground-based observations. Locations with HCHO concentrations above 8×10^{15} molec/cm^2 show a low bias of ~-31%. Conversely, clean sites with HCHO concentrations below 2.5×10^{15} molec/cm^2 undergo a high bias of 26%. Vigouroux et al. [2020] expanded the validation suite by including more than 25 FTIR stations located over both pristine and polluted sites. Results from the comparison with FTIR measurements (over clean areas) also indicate a high bias, whereas those compared in polluted areas show a low bias. By compiling numbers quoted in Lambert et al. [2020] and Vigouroux et al. [2020], we correct the existing biases in TROPOMI HCHO by scaling 25% ($<2.5\times10^{15}$ molec/cm^2) down columns in clean areas and 30% ($>=8\times10^{15}$ molec/cm^2) up in polluted areas. We assume the constant term of errors (e_{const}) to be equal to 4% of HCHO total columns based on Vigouroux et al. [2020].

2.1.3. MODIS AOD

To improve the simulation of total aerosol mass, we use the collection 6 MODIS aerosol optical depth (AOD) from both Aqua (~ 13:30 LT) and Terra (~ 10:30 LT) platforms over both land and ocean [Levy et al., 2013] (available at https://ladsweb.modaps.eosdis.nasa.gov, access May 2020). We independently validate all three major products, namely the deep blue, the dark target and a combined dark blue products by comparing to AOD values measured by AERONET over Europe at the same time period of this study. Only good and very good (qa>=2) pixels are selected for the comparison. The AERONET AOD data are computed based on the values at 500 nm and Angstrom Exponent in the 440-675 nm range. We collocate two datasets if they are within 10 km radius and less than 30 mins apart. The dark blue product results in the best agreement (r>0.87) with a high bias of <0.05 (Figure S1, and S2), and is available over both water and land. This product is therefore chosen for the data assimilation. We remove the bias and assign the value of the covariance matrix of observations to the RMSE values obtained from the comparison.

2.2. Surface Measurements

UV photometry and chemiluminescence surface ozone and NO_2 measurements all over continental Europe are used to investigate possible changes in their concentrations induced by the lockdown (https://discomap.eea.europa.eu/map/fme/AirQualityExport.htm, access June 2020). The NO_2 chemiluminescence measurements are usually overestimated due to interferences from the NO_z family (PAN, organic nitrate, HNO_3, etc.). We assume that the interferences are not significantly different between the baseline and lockdown mainly due to relatively low photochemistry in early spring [Lamsal et al., 2008] compared to summertime. Additionally, the correction needs a careful evaluation of the model with regards to the NO_z family whose measurements are not available in this case study.

More than 6450 meteorological stations archived on NOAA's integrated surface database (https://www.ncei.noaa.gov/data/global-hourly/, access April 2020) are used to validate the performance of our weather model in terms of several prognostic inputs including ambient air temperature, air humidity, and U and V wind components.

2.3. WRF-CMAQ Modeling

The regional air quality simulations at 15×15 km^2 are carried out with the widely used CMAQ v5.2.1 (https://doi.org/10.5281/zenodo.1212601) in conjunction with WRF v3.9.1 [Skamarock et al. 2008] models. The models overlap and cover continental Europe and some portions of Africa and Middle East. The domain consists of 483 east-west, 383 north-south grids, and 37 unevenly spaced eta levels (Figure 1). The simulation time period is from March to May 2019 and 2020 (six months). Since IC/BC are taken from already spun-up National Centers for Environmental Prediction (NCEP) FNL (final) reanalysis and

GEOS-Chem v12.9.3 (10.5281/zenodo.3974569) runs, we only spin up the models for the month of February. The chemistry configuration of the CMAQ model mainly consists of CB05 with chlorine chemistry (gases) and AERO6 (aerosol). Hourly-basis biogenic emissions are processed by the offline standalone Model of Emissions of Gases and Aerosols from Nature (MEGAN) v2.1 model [Guenther et al., 2012] based on high-resolution plant functional maps made by Ke et al. [2012]. The biogenic emission factors are estimated based on the PFT-specific information provided in Guenther et al. [2012]. The biogenic VOCs include a wide range of compounds including isoprene, monoterpenes, aromatic VOCs, and methanol. Soil NO_x emissions are estimated by Yienger and Levy, [1999]. Lightning NOx emissions are based on in-line calculations involving convective precipitation rates and cloud vertical distributions. Lightning NO_x emissions are not constrained in the model. Anthropogenic emissions are based on the Community Emissions Data System (CEDS) inventory in 2014 [Hoesly et al., 2018]. Diurnal scales are not considered for the anthropogenic emissions. We also output the CMAQ integrated process analysis quantifying the contribution of each process to the amount of compounds. The physical setting of WRF includes the Lin microphysics scheme [Lin et al., 1983], the Grell 3-D ensemble cumulus scheme [Grell and Dévényi, 2002], the RRTMG radiation scheme, ACM2 planetary boundary layer parametrization [Pleim, 2007], and Pleim-Xu land-surface scheme [Xiu and Pleim, 2001]. To minimize the deviation of the model from the reanalysis data, we turn on the grid nudging option with respect to wind, moisture, and temperature only outside of the PBL region. The inclusion of this option outside of the PBL is because we do not want the coarse reanalysis data washes out the relatively high-resolution dynamics. Moreover, leaf area index and the sea surface temperature are updated every 6 hours based on satellite measurements included in the reanalysis data. Extensive model evaluations based upon surface observations show a striking correspondence (Table S1, S2) which is indicative of fair energy budget and transport in our model.

2.4. Inverse Modeling and Data Assimilation

To adjust the bottom-up emission inventories, we follow a non-linear joint inversion method proposed in Souri et al. [2020a]. Briefly, a Gauss-Newton algorithm is utilized to incrementally solve the Bayes' quadratic function in analytical fashion. The posterior emissions are then derived by

$$\mathbf{x}_{i+1} = \mathbf{x}_a + \mathbf{G}[\mathbf{y} - F(\mathbf{x}_i) + K_i(\mathbf{x}_i - \mathbf{x}_a)] \tag{2}$$

where $\boldsymbol{y}$ is bias-corrected monthly-averaged TROPOMI NO_2 and HCHO observations, $\mathbf{x}_a$ (or $\mathbf{x}_0$) is the prior emissions, $\mathbf{x}_i$ is the posterior emission at the *i*th increment, F is the forward model (here WRF-CMAQ) to project the emissions onto columns space, **G** is the Kalman gain,

$$\mathbf{G} = \mathbf{S}_e\ K_i^T\left(K_i\mathbf{S}_e\ K_i^T + \mathbf{S}_o\ \right)^{-1} \tag{3}$$

and K_i (= $K(\mathbf{x}_i)$) is the Jacobian matrix calculated explicitly from the model using the finite difference method by perturbing separately NO_x and VOC emissions by 20%. The perturbations are applied for each iteration. The model outputs along with Jacobians and emissions are spatiotemporally co-registered with the observations. and $\mathbf{S}_e$ are the error covariance matrices of the observations and emissions. Similar to Souri et al. [2020a], the prior errors in anthropogenic NO_x and VOCs emissions are set to 50% and 150%, respectively. In terms of the biogenic emissions, the errors are set to 200% for both NO_x and VOCs. The instrument covariance matrices are populated with squared-sum of the aforementioned errors based on the compilation of the validation studies and precision errors provided with the data (Eq.1). Both error matrices are assumed diagonal. The inversion window is monthly meaning we have three separate correction factors in months of March, April, and May. The covariance matrix of the a posteriori is calculated by:

$$\hat{\mathbf{S}}_e = (\mathbf{I} - \mathbf{G}\hat{K}\quad)\mathbf{S}_e \tag{4}$$

where $\hat{K}$ is the Jacobian from the i*th* iteration. Here we iterate Eq.2 three times. The averaging kernels (**A**) are given by:

$$\mathbf{A} = \mathbf{I} - \hat{\mathbf{S}}_e\mathbf{S}_e^{-1} \tag{5}$$

Not only does this method considers non-linear chemical feedback among NO_2-HCHO-NO_x-VOC by simultaneously incorporating the HCHO and NO_2 in the inversion framework, it also permits quantification of **A** that explicitly explains the amount of information obtained from the observation. Low **A** indicates low **G** making the a posteriori to be rather independent of the observational constraint.

We also correct total aerosol mass by daily assimilating the MODIS dark blue AOD observations following the algorithm discussed in Jung et al. [2019]. Briefly, the assimilation framework uses a modified optimal interpolation method adjusting uniformly all relevant aerosol masses in a column as a function of a weighted-distance and appropriate errors.

3. Results and Discussion

3.1. Variability of HCHO and NO_2 columns seen by TROPOMI

We assess difference maps of TROPOMI HCHO and NO_2 columns in 2020 with respect to those in 2019 during the months of March, April and May. The difference maps along with the absolute values of the tropospheric NO_2 columns are shown in Figure 2. Regardless of the year, we observe a noticeable reduction in NO_2 as we approach warmer months which can be explained by increases in OH concentrations (higher water vapor content, solar radiation, and O_3 levels), faster vertical mixing due to larger sensible fluxes (more diluted columns for a given receptor due having a greater chance of experiencing stronger winds in higher altitudes), and a reduction in temperature-dependent light-duty diesel NO_x emissions [Grange et al., 2019]. This sequential decline of NO_2 obscures the quantitative interpretation of the satellite observations in two ways: first, as noted by Silvern et al. [2019], the free tropospheric background NO_2, which are highly uncertain, becomes comparable to those located at near-surface, and second, the relatively lower signal-to-noise ratios reduce the amount of information obtained for NO_x estimates (discussed later).

The anomaly map (2020 vs 2019) in March indicates pronounced decreases in tropospheric NO_2 columns over several countries including France, Spain, Italy, and Germany (box A). In contrast, we see increases in the magnitude of the NO_2 columns over some portions of the UK excluding London (box B), northeastern Germany (box C), and Moscow, Russia (box D). A very recent study [Barré et al. 2020] observed roughly the same tendency which was attributable to meteorological changes. While those changes are indeed an important piece of information, we should recognize that the degree of the enforced restrictions varies both spatially and temporally; moreover changes in emission heavily rely on the dominant emission sector (e.g., mobile or industry). For instance, according to TASS press [https://tass.com/society/1144123, accessed Sep 2020], Russian governments did not take significant measures to control the virus before April 15, immediately evident in the large NO_2 enhancement over Moscow in March (box D). During the next two months (April and May), we observe a major turnaround over this city (box F and H). In May, the anomaly of the tropospheric NO_2 suggests that the reduction in NO_x emissions abruptly experiences a hiatus in central Europe (box G). However it is crucial to note that these maps are based upon sporadic clear-sky pixels that might obscure the full portrayal of emissions changes happening throughout the period (discussed later).

We further investigate the changes in HCHO total columns shown in Figure 3 in the same context as we discussed for NO_2. Various VOCs with different sources contribute to the formation of HCHO (see Figure 2 in Chan Miller et al. [2016]). In theory, it is easier to single out anthropogenic-derived HCHO concentration by HCHO measurements made in wintertime, although temperature and photochemistry are always key influencers of oxidizing/photolyzing all types of VOCs. The inevitable trade-off for this is dealing with a weaker signal that is near to instrument detection limit. The TROPOMI HCHO retrieval offers a low detection limit for individual pixels (7×10^{15} molec/cm^2) that can be further lowered down by co-adding measurements (roughly a factor of $1/\sqrt{n}$). Accordingly, we observe a promising signal in March over eastern European countries that is not explainable by biogenic emissions; but the magnitudes of the difference over these areas ($<1.5\times10^{15}$ molec/cm^2) are below the detection limit ($\sim2.4\times10^{15}$ molec/cm^2 given the co-added measurements over time).

In April, results show elevated HCHO concentrations in high latitudes in 2019 (box I), mainly a result of biomass burning activities in eastern Europe [e.g., Karlsson et al. 2013; https://earthobservatory.nasa.gov/global-maps/MOD14A1_M_FIRE, accessed June 2020]. As temperature rises in May, the footprint of biogenic emissions become more visible. This signal is not only induced by the inherent temperature-dependency of biogenic emissions, but also stems from faster isoprene oxidation through higher levels of OH [Pusede et al. 2015]. The dipole anomaly of HCHO columns suggested by TROPOMI (box J and K) pertains largely to variations in ambient surface air temperature (discussed later).

3.2. Top-Down estimates of NO_x and VOC emissions

Following the inversion and the data assimilation frameworks, we adjust the total amounts of VOC, NO_x emissions, and aerosols mass using the well-characterized TROPOMI HCHO, NO_2 and MODIS AOD observations for the study time period. We focus on the topic of gas phase chemistry (i.e., ozone and its precursors) implying that the aerosol data assimilation is carried out to partially remove errors associated with radiation [e.g., Jung et al., 2019] or heterogenous chemistry [Jacob, 2000], therefore, the aspect of aerosol changes induced by the lockdown will be examined in a separate study. The spatial distributions of magnitude of the top-down NO_x and VOC emissions (i.e., constrained by the observations), their corresponding changes and averaging kernels are shown in Figure 4 and Figure 5, respectively. Moreover, the monthly values of a posteriori and the a priori are shown in Figure S3, S4, S5, and S6. It is worth emphasizing that we use identical prior values in terms of anthropogenic emissions in both years.

According to Figure 4, large averaging kernels associated with NO_x emissions are confined in high-emitting regions suggesting that the most valid estimates can be found in areas undergoing strong TROPOMI NO_2 signals. We observe a large improvement (31-45%) in the bias associated with simulated surface NO_2 using the posterior emissions compared to the surface measurements in many places around Europe with an exception to northeastern Germany where TROPOMI NO_2 observations deviates the model from the measurements (Figs S7, S8, S9 and 10). The improvements in correlation are minimal indicating that the prior location of emissions are well known. The discrepancies between the simulated tropospheric NO_2 columns versus TROPOMI are largely mitigated by the inversion (Figure S11 and S12). Immediately apparent in Figure 4 is a strong correlation between anomaly maps of TROPOMI tropospheric NO_2 (Figure 2) and those of top-down emissions. We observe reductions in NO_x emissions in March (14-31%) in several major cities including Paris, London, Madrid, and Milan; the reductions further expand to Rome, Brussels, Frankfurt, Warsaw, Kyiv, Moscow, and Belgrade with higher magnitudes (34-51%) in April. Table 2 summarizes the absolute and relative differences in total NO_x emissions estimated by the inversion binned to different regions in Europe based on country land borders. In general, the level of NO_x reduction is somewhat higher in April relative to months of March and May possibly due to temporal variabilities associated with the restrictions; for example, UK and Poland governments enforced the restrictions starting in the last week of March to the middle of April (see Figure S1 in Okruszek et al. [2020]; https://www.bbc.com/news/uk-51981653, accessed in March 2020). The decreased anthropogenic NO_x emissions in the strait of Gibraltar and Alboran Sea reveal reportedly reduced ship activities [United Nations Conference on Trade and Development Report, Accessed Dec 2020]. The numbers in May indicate that several countries in central and eastern Europe (shown in box G in Figure 2) likely eased coronavirus lockdown restrictions, a picture that has yet to be verified by surface measurements (discussed later).

As to VOC emissions, we observe improvements in the magnitude and spatial distribution of simulated HCHO columns after the inversion with respect to TROPOMI data over areas with a practical amount of information (e.g., AK>0.2) (Figure S13 and S14). It is very evident that the magnitudes of the emissions primarily follow anthropogenic sources in March; very low averaging kernels over major European cities in this month are indicative of inadequacies of one-month averaged TROPOMI HCHO data.

The inversion partly corrects for the large underrepresentation of biomass burning emissions in high latitudes occurring in April 2019 but due to large uncertainties of the retrieval over this area, averaging kernels are low. Vigouroux et al. [2020] showed FTIR HCHO columns to be around 4-6×10^{15} molec/cm^2 in Saint Peterburgh (59.9°N), Kiruna (67.8°N), and Sodankylä (67.4°N) in April 2019. Despite some improvements over the biomass burning areas in April 2019, the model still greatly underestimate HCHO columns suggesting more observations are needed to adjust the emissions. The predominately high pressure system formed over these areas in April 2019 (Figure S15) impedes the transport of the biomass burning pollution to central Europe.

The inversion suggests larger VOC emission rates in April 2020 compared to April 2019 over central Europe. Ordóñez et al. [2020] reported ambient temperature along with solar radiation to be higher than the norm. This is primarily due to a well-developed high-pressure system over the region (Figure S15) resulting in elevated HCHO columns. The top-down estimate is indicative of too low prior VOC emission rates over this area in April 2020. Given the significant role of VOCs in the formation of ozone in urban settings, this correction with reasonable AK (~0.4) is crucial for precisely modeling the surface ozone anomalies (shown later).

We revisit the pronounced dipole anomaly of dominantly biogenic VOC emissions in May. In this month, the biogenic VOCs dominate. Our model suggests that ambient surface temperature differences between Russian and central Europe are more than 7°C, possibly inducing a strong dipole anomaly in biogenic emissions. It is readily evident from the averaging kernels that more realistic information from TROPOMI HCHO is attainable in warmer months, contrary to the NO_2 case.

3.3. Disparities in near-surface concentrations suggested by the constrained model versus those by in-situ measurements

3.3.1. NO_2 and HCHO

It is necessary to examine whether the constrained model can adequately represent the changes observed by surface measurements. Unfortunately we limit the analysis to NO_2 due to the lack of routinely measured HCHO observations. Several factors can complicate this analysis: i) having overconfidence in the constrained model where the satellite observations used were uncertain; this problem can be safely addressed by only considering grid cells whose averaging kernels are above a threshold (here 0.5), ii) not accounting for spatial representivity function when it comes to directly comparing two datasets at different scales (i.e., point measurements vs the model grids); a statistical construction of the spatial representivity function [Janic et al., 2016] requires a dense observational network so that we can build a semivariogram; instead, we only consider model grid cells having more than two stations; those observations then are then averaged, iii) interferences of the NO_z family on NO_2 chemiluminescence measurements [Dickerson et al., 2019] which can be partly discounted when calculating differences, iv) model uncertainties, especially with respect to turbulent and convective fluxes that are heavily determined by representing local heterogeneity of forces and non-hydrostatic dynamics [Emanuel, 1994], all of which are challenging to properly resolve in a 15-km resolution.

With these caveats in mind, we plot the daily-averaged changes of surface NO_2 concentrations in 2020 relative to 2019 derived by the model and the European air quality network for the months of March, April, and May (Figure 6). Large gaps in Figure 6 are caused by considering grid cells with averaging kernels>0.5 and number of samples>2. The constrained model correlates reasonably well with the changes observed by the surface measurements in March and April, but it fails to reflect those in May. The surface measurements in March reinforce increases (or negligible changes) in NO_2 in northeastern Germany and UK, although the magnitudes are not as large as those suggested by the model. The constrained model tends to consistently underrepresent the decline in NO_2 in March (model: -11±21%, observation: -19±16%), April (model: -21±17%, observation: -29±21%), and May (model: -12±18%, observation: -25±20%). The frequency of TROPOMI data heavily impacted by cloudiness is another factor that can effectively lead to the underrepresentation of the model in a course of a month. Figure 7 depicts the average number of days that TROPOMI was able to sample on in both years (individual years are shown in Figure S16 and S17). There is a strong degree of correlation between the frequency of the data and the discrepancy between the model versus the surface observations. This is especially the case for May when we see too few days to be able to realistically reproduce NO_2 changes.

Given the reasonable performance of our model at reproducing the changes observed over the surface in April, a result of abundant samples from TROPOMI, we only focus on this month for the subsequent analysis.

3.3.2. Ozone

Figure 8 depicts the changes in maximum daily 8 h average (MDA8) surface ozone concentrations suggested by the measurements and the constrained model in April. Immediately obvious from the observations is the elevated surface ozone concentrations up to 32% in places where NO_x emissions drastically decreased such as Germany, Italy, France, UK, Switzerland, and Belgium (shown as box L). This tendency potentially driven by ozone chemistry [Sicard et al., 2020a; Shi and Brasseur, 2020; Grange et al. 2020; Salma et al., 2020; Lee et al., 2020] and/or meteorology [Lee et al., 2020; Wyche et al., 2021; Ordóñez et al., 2020] has drawn much attention. The challenge is to set up a model that is the characteristic of such a complex tendency [e.g., Parrish et al., 2014]. Encouragingly, our constrained model does have skill in describing the ozone enhancements over the whole domain (r=0.43). In the proximity of central Europe (shown as box L), the enhanced MDA8 ozone concentration observed by the observations is 7.35±11.27% (+3.76 ppbv) which is nearly a factor of two larger than that of the model (3.73±3.94%, +1.79 ppbv).

We plot the simulated MDA8 surface ozone concentrations in April 2020 (lockdown), April 2019 (baseline), and their differences in Figure 9. Surface ozone concentrations show a strong latitudinal gradient with lower values in higher latitudes, underscoring the importance role of solar radiation in the formation of ozone. Meanwhile, the Mediterranean basin is prone to elevated concentrations of ozone resulting from different factors including calm weather, the transport from neighboring countries, atmospheric recirculation in coastal environments, and local emissions [Lelieveld et al., 2002]. While we observe a strong variability in the difference map, signaling various sources and sinks (discussed later), three distinctive features in 2020 in comparison to 2019 are evident: i) higher concentrations over the central Europe (up to 5 ppbv), ii) lower concentrations in eastern Europe (-2.67±1.65 ppbv) due to the 2019 biomass burning activities and larger snow cover fraction accelerating photolysis [e.g., Rappenglück et al., 2014], and iii) lower values in the Iberian Peninsula (-0.51±1.41 ppbv) [Ordóñez et al., 2020].

While the remaining model uncertainty could be either improved or characterized by including more observations (if available), reconfiguring the physical/chemical mechanisms used, and constraining chemical boundary conditions, it is imperative to gauge the contribution of each process (i.e., transport, chemistry, etc.) in forming ozone changes. Here we mainly make use of the CMAQ process analysis. A direct use of the process analysis output (in unit of ppbv hr^{-1}) can be confusing as both physical/chemical processes and underlying concentrations are inextricably linked together. To be able to isolate each process (in unit of hr^{-1}), we normalize the outputs by ozone concentrations. We average each process at the same hours used in calculating MDA8. Figure 10 shows the major model processes, namely horizontal transport (horizontal advection plus diffusion), vertical transport (vertical advection plus diffusion), dry deposition, and chemistry in 2020, 2019, and their differences. Positive (negative) values indicate a source (sink) for ozone. Regarding the horizontal transport, the values mostly follow the transport pattern and are dependent on whether the advected air mass is more or less polluted. The vertical transport correlates with the PBLH which is an indicator of the atmospheric stability and turbulence, although we should not rule out the impact of the subgrid convective transport that can occur sporadically. Low PBLHs are usually associated with more stable (or sometimes capping inversion) and weaker vertical mixing [e.g., Nevius and Evans, 2018]. Vertical transport which is majorly dictated by the vertical diffusion is by far the most influential factor in the magnitude of ozone [e.g., Cuchiara et al., 2014]. In contrast to NO_2 and HCHO, a stronger vertical diffusion increases surface ozone due to positive gradients of ozone with respect to altitude. However, the aerodynamic resistance controlling dry deposition velocity [Seinfield and Pandis, 2006] is also a function of turbulent transport. For example, during daytime, intensified turbulence exposes more pollution to surface deposition. It is because of this reason that we see the dry deposition process largely counteracting vertical transport. This will leave the chemistry process the major driver of the ozone changes.

We separately sum the quantities of the physical processes and PO_3 contributing to MDA8 surface ozone changes binned to box L. The physical processes lead to -4.83 ppbv changes in the MDA8 ozone mainly due to a relatively larger dry deposition in 2020, whereas $P(O_3)$ contributes to +5.89 ppbv. The net effect is +1.06 ppbv which is slightly smaller than the simulated changes in MDA8 ozone in this region (+1.79 ppbv). This apparent discrepancy is caused by the differences in boundary and initial conditions which are not quantifiable by the process analysis and would require additional sensitivity test. Nonetheless, we believe these numbers should provide convincing evidence on the fact that chemistry has promoted the enhancements of surface ozone during the lockdown.

Chemistry is also a function of meteorology, specifically solar radiation and temperature. A typical scenario to isolate emissions from meteorology is by running the model with fixed anthropogenic emissions (and boundary conditions) and subtracting the outputs from the variable emission output. Figure 11 shows the contribution of anthropogenic emissions (VOCs and NO_x) to the changes seen over the surface. The anthropogenic emissions make up roughly 58% of the changes. The map is strongly in line with the changes in NO_x emissions constrained by TROPOMI. The impact of meteorology plus biogenic changes (the former is dominant) highly correlates with anomalies in both surface air temperature and photolysis rate (not shown). We observe negligible ozone changes due to emissions over Iberian Peninsula reinforcing the significance of the meteorological impacts [Ordóñez et al., 2020].

3.4.Ozone chemistry

Figure 12 shows the numerically-solved ozone production rates (PO_3) simulated by the constrained model during the MDA8 hours period. We observe positive PO_3 in less polluted areas and eastern Europe where biomass burning activities occurred in 2019, while negative PO_3 in major cities. Negative values in PO_3 are indicative of either loss in O_3 or O_3-NO-NO_2 partitioning. The difference in PO_3 between the two years suggests that the ozone enhancement in box L is caused by a reduction in negative PO_3 in 2020 over major cities compared to 2019. To examine which pathways are contributing to this pattern, we attempt to analytically reproduce the numerically-solved PO_3 (Figure 12) through two different equations: the first equation widely applied in photochemically active environments follows [Kleinman et al., 2002]:

$$\begin{aligned} P(O_3) = {} & k_{HO_2+NO}[HO_2][NO] + \sum k_{RO_{2i}+NO}[RO_{2i}][NO] \\ & - k_{OH+NO_2+M}[OH][NO_2][M] - k_{HO_2+O_3}[HO_2][O_3] \\ & - k_{OH+O_3}[OH][O_3] - k_{O(^1D)+H_2O}[O(^1D)][H_2O] - L(O_3 \\ & + VOCs) \end{aligned} \tag{6}$$

This equation yields negative values only if the O_3 loss pathways including NO_2+OH, HO_x+O_3 , O^1D+H_2O and O_3+VOCs dominate over the first two terms. The second equation which is independent of RO_2 and HO_2 concentrations [Thornton et al., 2002], is:

$$P(O_3) = jNO_2[NO_2] - k_{NO+O_3}[O_3][NO] \tag{7}$$

In summer, this equation tends to be positive during early afternoon, almost zero during afternoon (steady-state), and negative in early morning (or night) in which the second term (O_3 titration) is leading. Any abrupt changes in NO_x and VOC, and photolysis can directly affect Eq.7 moving PO_3 out of the diel steady-state. The assumption of the steady-state (PO_3 from Eq.7 equals to zero) is also not valid if an air parcel is in the vicinity of high-emitting NO_x sources [Thornton et al., 2002].

Figure 13 displays the reactions rates of each individual component involved in Eq.6 averaged during the MDA8 hours. HO_2+NO is the dominant chemical source of ozone correlating well with the changes in NO_x and prevailing chemical conditions regimes (NO_x-sensitive vs VOC-sensitive). Souri et al. [2020a] found the reaction of RO_2+NO to be primarily dependent on VOCs. Likewise, we observe a strong degree of correlation between the anomaly of RO_2+NO and that of VOCs (Figure 5). Figure 13 indicates that the chemical pathways of ozone loss are rather constant between the two years; therefore the largely negative PO_3 over urban areas shown previously in Figure 12 is not reproducible using this equation. Figure 14 shows the reactions rates of $J_{NO2}[NO_2]$, $k_{NO+O3}[NO][O_3]$, and the difference during the MDA8 hours. The difference maps replicate the largely negative PO_3 over cities suggesting that we are not in the diel steady-state, and O_3 titration is prevailing due to relatively low photochemistry in the springtime. Table 3 lists the averaged reactions rates involved in Eq.6 and 7 along with the numerically-solved PO_3 shown in Figure 12 over box L. These numbers suggest that the major chemical pathways of enhanced ozone are through $J_{NO2}[NO_2]$ and $k_{NO+O3}[NO][O_3]$, implying that O_3-NO-NO_2 partitioning is more consequential than other chemical pathways. This analysis strongly coincides with Lee et al. [2020] and Wyche et al. [2021] who observed roughly constant O_3+NO_2 concentrations over the UK before and during the lockdown 2020.

4. Summary

The slowdown in human activities due to the COVID-19 pandemic had an immediate and sweeping impact on air pollution over Europe [Barré et al. 2020; Siccard et al., 2020]. Satellite monitoring systems with large spatial coverage help shed light on the spatial and temporal extent of those impacts. The relationships between satellite-derived HCHO and NO_2 columns and near-surface emissions have proven difficult to fully establish without using realistic models, capable of providing insights on the convoluted processes involving chemistry, dynamics, transport, and photochemistry and therefore help with deciphering what anomaly maps of satellite concentrations are suggesting [e.g., Goldberg et al., 2020]. To address these challenges, we jointly constrained NO_x and VOC emissions using TROPOMI HCHO and NO_2 columns following a non-linear Gauss Newton method developed in Souri et al. [2020a], in addition to assimilating MODIS AOD observations based on Jung et al. [2019]. The constrained emissions also permitted investigating the simultaneous effects of physical and chemical processes contributing to ozone formation, illuminating the complexities associated with non-linear chemistry.

Several implications of the derived emissions for the months of March, April, and May 2020 (lockdown) relative to those in 2019 (baseline) were investigated. First, as previously reported [Sicard et al., 2020; Barré et al. 2020], we observed a significant reduction in NO_x in March (14-31%) in several major polluted regions including Paris, London, Madrid, and Milan. The reductions were further seen in other cities such as Rome, Brussels, Frankfurt, Warsaw, Belgrade, Kyiv, and Moscow (34-51%) in April. Second, a large temporal variability associated with the reduction in NO_x was evident, as each country possibly had different timeline of restrictions. For instance, NO_x emissions decreased drastically in April rather than March in UK, Moscow, and Poland. Fourth, changes in VOC emissions were primarily dictated by biogenic and biomass burning sources in April and May.

The constrained model calculations gave good representations of near-surface NO_2 changes in April (model: -21±17%, observation: -29±21%) in places where the top-down estimates are reasonable (averaging kernels > 0.5), but inferior representations in other months, especially in May (model: -12±18%, observation: -25±20%). This tendency mainly arose from TROPOMI frequencies; too few days (10-26%) in May due to cloudiness precluded the determination of realistic NO_x emission changes.

We observed surface MDA8 ozone increase from both model and measurements in April 2020 with respect to the baseline. Comparisons of calculation by the constrained model in terms of MDA8 surface ozone found reasonable agreement with observations in the proximity of central Europe in April (model: +3.73±3.94%, +1.79 ppbv, observation: +7.35±11.27%, +3.76 ppbv). These comparisons indicate that the performance of the constrained model to reproduce the ozone enhancement feature is promising, suggesting fruitful information in TROPOMI NO_2 and HCHO, although reasons behind the underestimation of the enhancement remained unexplained. It was clear that the dominantly negative ozone production rates dictated by O_3-NO-NO_2 partitioning ($J_{NO2}[NO_2]-k_{NO+O3}[NO][O_3]$) became less negative primarily due to the reduced NO_x emissions in urban areas where O_3 titration occurred. This tendency was in agreement with studies of Lee et al. [2020] and Wyche et al. [2021]. We found negligible differences in ozone production from $[HO_2+RO_2][NO]$ and ozone loss from O^1D+H_2O and O_3+HO_x between the two years suggesting photochemistry was rather low in the springtime over Europe.

We further quantified the contributions of physical processes (transport, diffusion and dry deposition) and chemistry to the formation/loss of ozone using the integrated process rates. The physical processes decreased MDA8 ozone by -4.83 ppbv resulting from relatively larger dry deposition in 2020, whereas chemistry (ozone production) augmented ozone levels by +5.89 ppbv, indicating that rising ozone was primarily impacted by changes in chemistry. Enhanced air temperature and photolysis in 2020, both of which were well captured in our model, also affected chemistry. Experiments with fixed anthropogenic emissions underwent significant enhancement in surface MDA8 ozone over central Europe, but those only contribute to 42% of the total enhancement indicating that anthropogenic emissions were the major factor.

The results shown here reveal previously unquantified characteristics of ozone and its precursors emission changes during the lockdown 2020 in Europe. We have been able to measure the amount of changes along with the level of confidence in NO_x and VOC emissions using a state-of-the-art inversion technique by leveraging well-characterized satellite observations, which in turn, allowed us to unravel the chemical and physical processes contributing to increased ozone in Europe. Unless a comprehensive air quality campaign targeting COVID-19 related lockdown is available, we recommend that the impact of lockdown on air pollution should be examined through the lens of well-established models constrained by publicly available data, especially those from space in less cloudy environments.

Author contributions

AHS designed the research, analyzed the data, conducted the inverse modeling and atmospheric modeling (for CMAQ, GEOS-Chem, WRF, and MEGAN), made all figures, and wrote the paper. JB validated WRF-CMAQ model and reformatted the surface observation files. CRN and GGA did literature review regarding the TROPOMI validation. YJ validated MODIS AOD. DW helped with implementing the AOD assimilation framework. KC, JM, and XL guided the discussion. All authors contributed to discussion and edited the paper.

Data availability

The atmospheric inversion data are publicly available from Souri et al. [2021]. The model outputs are available upon the request from ahsouri@cfa.harvard.edu. The links on where to download surface and satellite observations that are used in this study are already provided in the text.

Acknowledgments

Amir H. Souri acknowledges supports from the Smithsonian Astrophysical Observatory (SAO) Scholarly Award (40488100AA50203), MethaneSAT LLC, and Environmental Defense Fund. J. Bak acknowledges Basic Science Research Program through the National Research Foundation of

Korea (NRF) funded by the Ministry of Education (2020R1A6A1A03044834). Both calculations and simulations are done on the Smithsonian Institution High-Performance Cluster (SI/HPC) (https://doi.org/10.25572/SIHPC). The views expressed in this manuscript are those of the authors alone and do not necessarily reflect the views and policies of the U.S. Environmental Protection Agency. EPA does not endorse any products or commercial services mentioned in this publication.

References

Auligné, T., McNally, A. P., and Dee, D. P.: Adaptive bias correction for satellite data in a numerical weather prediction system, Quarterly Journal of the Royal Meteorological Society, 133, 631–642, https://doi.org/10.1002/qj.56, 2007.

Barré, J., Petetin, H., Colette, A., Guevara, M., Peuch, V.-H., Rouil, L., Engelen, R., Inness, A., Flemming, J., Pérez García-Pando, C., Bowdalo, D., Meleux, F., Geels, C., Christensen, J. H., Gauss, M., Benedictow, A., Tsyro, S., Friese, E., Struzewska, J., Kaminski, J. W., Douros, J., Timmermans, R., Robertson, L., Adani, M., Jorba, O., Joly, M. and Kouznetsov, R.: Estimating lockdown induced European NO_2 changes, Atmospheric Chemistry and Physics Discussions, 1–28, https://doi.org/10.5194/acp-2020-995, 2020.

Baudic, A., Gros, V., Sauvage, S., Locoge, N., Sanchez, O., Sarda-Estève, R., Kalogridis, C., Petit, J.-E., Bonnaire, N., Baisnée, D., Favez, O., Albinet, A., Sciare, J. and Bonsang, B.: Seasonal variability and source apportionment of volatile organic compounds (VOCs) in the Paris megacity (France), Atmospheric Chemistry and Physics, 16(18), 11961–11989, https://doi.org/10.5194/acp-16-11961-2016, 2016.

Bekbulat, B., Apte, J. S., Millet, D. B., Robinson, A. L., Wells, K. C., Presto, A. A., and Marshall, J. D.: Changes in criteria air pollution levels in the US before, during, and after Covid-19 stay-at-home orders: Evidence from regulatory monitors, Science of The Total Environment, 769, 144693, https://doi.org/10.1016/j.scitotenv.2020.144693, 2021.

Boersma, K. F., Eskes, H. J., Richter, A., De Smedt, I., Lorente, A., Beirle, S., van Geffen, J. H. G. M., Zara, M., Peters, E., Van Roozendael, M., Wagner, T., Maasakkers, J. D., van der A, R. J., Nightingale, J., De Rudder, A., Irie, H., Pinardi, G., Lambert, J.-C. and Compernolle, S. C.: Improving algorithms and uncertainty estimates for satellite NO_2 retrievals: results from the quality assurance for the essential climate variables (QA4ECV) project, Atmospheric Measurement Techniques, 11(12), 6651–6678, https://doi.org/10.5194/amt-11-6651-2018, 2018.

Castellanos, P. and Boersma, K. F.: Reductions in nitrogen oxides over Europe driven by environmental policy and economic recession, Scientific Reports, 2(1), 265, https://doi.org/10.1038/srep00265, 2012.

Chan Miller, C., Jacob, D. J., Marais, E. A., Yu, K., Travis, K. R., Kim, P. S., Fisher, J. A., Zhu, L., Wolfe, G. M., Hanisco, T. F., Keutsch, F. N., Kaiser, J., Min, K.-E., Brown, S. S., Washenfelder, R. A., González Abad, G. and Chance, K.: Glyoxal yield from isoprene oxidation and relation to formaldehyde: chemical mechanism, constraints from SENEX aircraft observations, and interpretation of OMI satellite data, Atmospheric Chemistry and Physics, 17(14), 8725–8738, https://doi.org/10.5194/acp-17-8725-2017, 2017.

Chan, K. L., Wiegner, M., van Geffen, J., De Smedt, I., Alberti, C., Cheng, Z., Ye, S. and Wenig, M.: MAX-DOAS measurements of tropospheric NO2 and HCHO in Munich and the comparison to OMI and TROPOMI satellite observations, Atmospheric Measurement Techniques, 13(8), 4499–4520, https://doi.org/10.5194/amt-13-4499-2020, 2020.

Cooper, M. J., Martin, R. V., Hammer, M. S., and McLinden, C. A.: An Observation-Based Correction for Aerosol Effects on Nitrogen Dioxide Column Retrievals Using the Absorbing Aerosol Index, 46, 8442–8452, https://doi.org/10.1029/2019GL083673, 2019.

Copernicus Sentinel data processed by ESA, German Aerospace Center (DLR) (2019), Sentinel-5P TROPOMI Tropospheric Formaldehyde HCHO 1-Orbit L2 5.5km x 3.5km, Greenbelt, MD, USA, Goddard Earth Sciences Data and Information Services Center (GES DISC), Accessed: [Data Access Date], https://doi.org/10.5270/S5P-tjlxfd2

Copernicus Sentinel data processed by ESA, Koninklijk Nederlands Meteorologisch Instituut (KNMI) (2019), Sentinel-5P TROPOMI Tropospheric NO2 1-Orbit L2 5.5km x 3.5km, Greenbelt, MD, USA, Goddard Earth Sciences Data and Information Services Center (GES DISC), Accessed: [Data Access Date], https://doi.org/10.5270/S5P-s4ljg54

Cuchiara, G. C., Li, X., Carvalho, J. and Rappenglück, B.: Intercomparison of planetary boundary layer parameterization and its impacts on surface ozone concentration in the WRF/Chem model for a case study in Houston/Texas, Atmospheric Environment, 96, 175–185, https://doi.org/10.1016/j.atmosenv.2014.07.013, 2014.

De Smedt, I., Theys, N., Yu, H., Danckaert, T., Lerot, C., Compernolle, S., Van Roozendael, M., Richter, A., Hilboll, A., Peters, E., Pedergnana, M., Loyola, D., Beirle, S., Wagner, T., Eskes, H., van Geffen, J., Boersma, K. F. and Veefkind, P.: Algorithm theoretical baseline for formaldehyde retrievals from S5P TROPOMI and from the QA4ECV project, Atmospheric Measurement Techniques, 11(4), 2395–2426, https://doi.org/10.5194/amt-11-2395-2018, 2018.

Dickerson, R. R., Anderson, D. C. and Ren, X.: On the use of data from commercial NOx analyzers for air pollution studies, Atmospheric Environment, 214, 116873, https://doi.org/10.1016/j.atmosenv.2019.116873, 2019.

Emanuel, K. A.: Atmospheric Convection, 1st edition., Oxford University Press, New York., 1994.

Fauci, A. S., Lane, H. C. and Redfield, R. R.: Covid-19 — Navigating the Uncharted, New England Journal of Medicine, 382(13), 1268–1269, https://doi.org/10.1056/NEJMe2002387, 2020.

Gaubert, B., Bouarar, I., Doumbia, T., Liu, Y., Stavrakou, T., Deroubaix, A., Darras, S., Elguindi, N., Granier, C., Lacey, F., Müller, J.-F., Shi, X., Tilmes, S., Wang, T., and Brasseur, G. P.: Global Changes in Secondary Atmospheric Pollutants During the 2020 COVID-19 Pandemic, 126, e2020JD034213, https://doi.org/10.1029/2020JD034213, 2021.

Goldberg, D. L., Anenberg, S. C., Griffin, D., McLinden, C. A., Lu, Z. and Streets, D. G.: Disentangling the Impact of the COVID-19 Lockdowns on Urban NO2 From Natural Variability, Geophysical Research Letters, 47(17), e2020GL089269, https://doi.org/10.1029/2020GL089269, 2020.

Grange, S. K., Farren, N. J., Vaughan, A. R., Rose, R. A. and Carslaw, D. C.: Strong Temperature Dependence for Light-Duty Diesel Vehicle NOx Emissions, Environ. Sci. Technol., 53(11), 6587–6596, https://doi.org/10.1021/acs.est.9b01024, 2019.

Grell, G. A. and Dévényi, D.: A generalized approach to parameterizing convection combining ensemble and data assimilation techniques, Geophysical Research Letters, 29(14), 38-1-38–4, https://doi.org/10.1029/2002GL015311, 2002.

Griffin, D., Zhao, X., McLinden, C. A., Boersma, F., Bourassa, A., Dammers, E., Degenstein, D., Eskes, H., Fehr, L., Fioletov, V., Hayden, K., Kharol, S. K., Li, S.-M., Makar, P., Martin, R. V., Mihele, C., Mittermeier, R. L., Krotkov, N., Sneep, M., Lamsal, L. N., Linden, M. ter, Geffen, J. van, Veefkind, P. and Wolde, M.: High-Resolution Mapping of Nitrogen Dioxide With TROPOMI: First Results and Validation Over the Canadian Oil Sands, Geophysical Research Letters, 46(2), 1049–1060, https://doi.org/10.1029/2018GL081095, 2019.

Guenther, A. B., Jiang, X., Heald, C. L., Sakulyanontvittaya, T., Duhl, T., Emmons, L. K. and Wang, X.: The Model of Emissions of Gases and Aerosols from Nature version 2.1 (MEGAN2.1): an extended and updated framework for modeling biogenic emissions, Geoscientific Model Development, 5(6), 1471–1492, https://doi.org/10.5194/gmd-5-1471-2012, 2012.

He, G., Pan, Y. and Tanaka, T.: The short-term impacts of COVID-19 lockdown on urban air pollution in China, Nature Sustainability, 3(12), 1005–1011, https://doi.org/10.1038/s41893-020-0581-y, 2020.

Hoesly, R. M., Smith, S. J., Feng, L., Klimont, Z., Janssens-Maenhout, G., Pitkanen, T., Seibert, J. J., Vu, L., Andres, R. J., Bolt, R. M., Bond, T. C., Dawidowski, L., Kholod, N., Kurokawa, J., Li, M., Liu, L., Lu, Z., Moura, M. C. P., O'Rourke, P. R. and Zhang, Q.: Historical (1750–2014) anthropogenic emissions of reactive gases and aerosols from the Community Emissions Data System (CEDS), Geoscientific Model Development, 11(1), 369–408, https://doi.org/10.5194/gmd-11-369-2018, 2018.

Jacob, D. J.: Heterogeneous chemistry and tropospheric ozone, Atmospheric Environment, 34(12), 2131–2159, https://doi.org/10.1016/S1352-2310(99)00462-8, 2000.

Jacobson, M. Z.: Fundamentals of Atmospheric Modeling, 2nd ed., Cambridge University Press, Cambridge., 2005.

Janjić, T., Bormann, N., Bocquet, M., Carton, J. A., Cohn, S. E., Dance, S. L., Losa, S. N., Nichols, N. K., Potthast, R., Waller, J. A. and Weston, P.: On the representation error in data assimilation, Quarterly Journal of the Royal Meteorological Society, 144(713), 1257–1278, https://doi.org/10.1002/qj.3130, 2018.

Judd, L. M., Al-Saadi, J. A., Szykman, J. J., Valin, L. C., Janz, S. J., Kowalewski, M. G., Eskes, H. J., Veefkind, J. P., Cede, A., Mueller, M., Gebetsberger, M., Swap, R., Pierce, R. B., Nowlan, C. R., Abad, G. G., Nehrir, A. and Williams, D.: Evaluating Sentinel-5P TROPOMI tropospheric NO2 column densities with airborne and Pandora spectrometers near New York City and Long Island Sound, Atmospheric Measurement Techniques, 13(11), 6113–6140, https://doi.org/10.5194/amt-13-6113-2020, 2020.

Jung, J., Souri, A. H., Wong, D. C., Lee, S., Jeon, W., Kim, J. and Choi, Y.: The Impact of the Direct Effect of Aerosols on Meteorology and Air Quality Using Aerosol Optical Depth Assimilation During the KORUS-AQ Campaign, Journal of Geophysical Research: Atmospheres, 124(14), 8303–8319, https://doi.org/10.1029/2019JD030641, 2019.

Jung, Y., González Abad, G., Nowlan, C. R., Chance, K., Liu, X., Torres, O., and Ahn, C.: Explicit Aerosol Correction of OMI Formaldehyde Retrievals, Earth and Space Science, 6, 2087–2105, https://doi.org/10.1029/2019EA000702, 2019.

Karlsson, P. E., Ferm, M., Tømmervik, H., Hole, L. R., Pihl Karlsson, G., Ruoho-Airola, T., Aas, W., Hellsten, S., Akselsson, C., Mikkelsen, T. N. and Nihlgård, B.: Biomass burning in eastern Europe during spring 2006 caused high deposition of ammonium in northern Fennoscandia, Environmental Pollution, 176, 71–79, https://doi.org/10.1016/j.envpol.2012.12.006, 2013.

Ke, Y., Leung, L. R., Huang, M., Coleman, A. M., Li, H. and Wigmosta, M. S.: Development of high resolution land surface parameters for the Community Land Model, Geoscientific Model Development, 5(6), 1341–1362, https://doi.org/10.5194/gmd-5-1341-2012, 2012.

Kleinman, L. I., Daum, P. H., Lee, Y.-N., Nunnermacker, L. J., Springston, S. R., Weinstein-Lloyd, J. and Rudolph, J.: Ozone production efficiency in an urban area, Journal of

Geophysical Research: Atmospheres, 107(D23), ACH 23-1-ACH 23-12, https://doi.org/10.1029/2002JD002529, 2002.

Krotkov, N. A., McLinden, C. A., Li, C., Lamsal, L. N., Celarier, E. A., Marchenko, S. V., Swartz, W. H., Bucsela, E. J., Joiner, J., Duncan, B. N., Boersma, K. F., Veefkind, J. P., Levelt, P. F., Fioletov, V. E., Dickerson, R. R., He, H., Lu, Z. and Streets, D. G.: Aura OMI observations of regional SO_2 and NO_2 pollution changes from 2005 to 2015, Atmospheric Chemistry and Physics, 16(7), 4605–4629, https://doi.org/10.5194/acp-16-4605-2016, 2016.

Lambert, J.-C., Compernole, S., Eichmann, K.-U., Graaf, M. de, Hubert, D., Keppens, A., Kleipool, Q., Langerock, B., Sha, M. K., Verhoelst, T., Wagner, T., Ahn, C., Argyrouli, A., Balis, D., Chan, K. L., Smedt, I. De, Eskes, H., Fjæraa, A. M., Garane, K., Gleason, J. F., Goutail, F., Granville, J., Hedelt, P., Heue, K.-P., Jaross, G., Koukouli, M., Landgraf, J., Lutz, R., Nanda, S., Niemejer, S., Pazmiño, A., Pinardi, G., Pommereau, J.-P., Richter, A., Rozemeijer, N., Sneep, M., Zweers, D. S., Theys, N., Tilstra, G., Torres, O., Valks, P., Vigouroux, C., Wang, P. and Weber, M.: Quarterly Validation Report of the Copernicus Sentinel-5 Precursor Operational Data Products #06: April 2018 - February 2020. http://www.tropomi.eu/sites/default/files/files/publicS5P-MPC-IASB-ROCVR-02.0.2-20190411_FINAL.pdf

Lamsal, L. N., Martin, R. V., Donkelaar, A. van, Steinbacher, M., Celarier, E. A., Bucsela, E., Dunlea, E. J. and Pinto, J. P.: Ground-level nitrogen dioxide concentrations inferred from the satellite-borne Ozone Monitoring Instrument, Journal of Geophysical Research: Atmospheres, 113(D16), https://doi.org/10.1029/2007JD009235, 2008.

Le Quéré, C., Jackson, R. B., Jones, M. W., Smith, A. J. P., Abernethy, S., Andrew, R. M., De-Gol, A. J., Willis, D. R., Shan, Y., Canadell, J. G., Friedlingstein, P., Creutzig, F. and Peters, G. P.: Temporary reduction in daily global CO 2 emissions during the COVID-19 forced confinement, Nature Climate Change, 10(7), 647–653, https://doi.org/10.1038/s41558-020-0797-x, 2020.

Le, T., Wang, Y., Liu, L., Yang, J., Yung, Y. L., Li, G. and Seinfeld, J. H.: Unexpected air pollution with marked emission reductions during the COVID-19 outbreak in China, Science, 369(6504), 702–706, https://doi.org/10.1126/science.abb7431, 2020.

Lee, J. D., Drysdale, W. S., Finch, D. P., Wilde, S. E. and Palmer, P. I.: UK surface NO_2 levels dropped by 42 % during the COVID-19 lockdown: impact on surface O_3, Atmospheric Chemistry and Physics, 20(24), 15743–15759, https://doi.org/10.5194/acp-20-15743-2020, 2020.

Lelieveld, J., Berresheim, H., Borrmann, S., Crutzen, P. J., Dentener, F. J., Fischer, H., Feichter, J., Flatau, P. J., Heland, J., Holzinger, R., Korrmann, R., Lawrence, M. G., Levin, Z., Markowicz, K. M., Mihalopoulos, N., Minikin, A., Ramanathan, V., Reus, M. de, Roelofs, G. J., Scheeren, H. A., Sciare, J., Schlager, H., Schultz, M., Siegmund, P., Steil, B., Stephanou, E. G., Stier, P., Traub, M., Warneke, C., Williams, J., and Ziereis, H.: Global Air Pollution Crossroads over the Mediterranean, 298, 794–799, https://doi.org/10.1126/science.1075457, 2002.

Levy, R. C., Mattoo, S., Munchak, L. A., Remer, L. A., Sayer, A. M., Patadia, F. and Hsu, N. C.: The Collection 6 MODIS aerosol products over land and ocean, Atmospheric Measurement Techniques, 6(11), 2989–3034, https://doi.org/10.5194/amt-6-2989-2013, 2013.

Li, K. and Lin, B.: Impacts of urbanization and industrialization on energy consumption/CO2 emissions: Does the level of development matter?, Renewable and Sustainable Energy Reviews, 52, 1107–1122, https://doi.org/10.1016/j.rser.2015.07.185, 2015.

Lin, Y.-L., Farley, R. D. and Orville, H. D.: Bulk Parameterization of the Snow Field in a Cloud Model, Journal of Applied Meteorology and Climatology, 22(6), 1065–1092, https://doi.org/10.1175/1520-0450(1983)022<1065:BPOTSF>2.0.CO;2, 1983.

Liu, F., Page, A., Strode, S. A., Yoshida, Y., Choi, S., Zheng, B., Lamsal, L. N., Li, C., Krotkov, N. A., Eskes, H., A, R. van der, Veefkind, P., Levelt, P. F., Hauser, O. P. and Joiner, J.: Abrupt decline in tropospheric nitrogen dioxide over China after the outbreak of COVID-19, Science Advances, 6(28), eabc2992, https://doi.org/10.1126/sciadv.abc2992, 2020.

Lorenz, E. N.: Deterministic Nonperiodic Flow, Journal of the Atmospheric Sciences, 20(2), 130–141, https://doi.org/10.1175/1520-0469(1963)020<0130:DNF>2.0.CO;2, 1963.

Marais, E. A., Jacob, D. J., Kurosu, T. P., Chance, K., Murphy, J. G., Reeves, C., Mills, G., Casadio, S., Millet, D. B., Barkley, M. P., Paulot, F. and Mao, J.: Isoprene emissions in Africa inferred from OMI observations of formaldehyde columns, Atmospheric Chemistry and Physics, 12(14), 6219–6235, https://doi.org/10.5194/acp-12-6219-2012, 2012.

Martin, R. V., Chance, K., Jacob, D. J., Kurosu, T. P., Spurr, R. J. D., Bucsela, E., Gleason, J. F., Palmer, P. I., Bey, I., Fiore, A. M., Li, Q., Yantosca, R. M., and Koelemeijer, R. B. A.: An improved retrieval of tropospheric nitrogen dioxide from GOME, 107, ACH 9-1-ACH 9-21, https://doi.org/10.1029/2001JD001027, 2002.

Miyazaki, K., Bowman, K., Sekiya, T., Jiang, Z., Chen, X., Eskes, H., Ru, M., Zhang, Y. and Shindell, D.: Air Quality Response in China Linked to the 2019 Novel Coronavirus (COVID-19) Lockdown, Geophysical Research Letters, 47(19), e2020GL089252, https://doi.org/10.1029/2020GL089252, 2020.

Nevius, D. S. and Evans, C.: The Influence of Vertical Advection Discretization in the WRF-ARW Model on Capping Inversion Representation in Warm-Season, Thunderstorm-Supporting Environments, Weather and Forecasting, 33(6), 1639–1660, https://doi.org/10.1175/WAF-D-18-0103.1, 2018.

Okruszek, Ł., Aniszewska-Stańczuk, A., Piejka, A., Wiśniewska, M., and Żurek, K.: Safe but Lonely? Loneliness, Anxiety, and Depression Symptoms and COVID-19, Front. Psychol., 11, https://doi.org/10.3389/fpsyg.2020.579181, 2020.

Ordóñez, C., Garrido-Perez, J. M. and García-Herrera, R.: Early spring near-surface ozone in Europe during the COVID-19 shutdown: Meteorological effects outweigh emission changes, Science of The Total Environment, 747, 141322, https://doi.org/10.1016/j.scitotenv.2020.141322, 2020.

Parrish, D. D., Lamarque, J.-F., Naik, V., Horowitz, L., Shindell, D. T., Staehelin, J., Derwent, R., Cooper, O. R., Tanimoto, H., Volz-Thomas, A., Gilge, S., Scheel, H.-E., Steinbacher, M. and Fröhlich, M.: Long-term changes in lower tropospheric baseline ozone concentrations: Comparing chemistry-climate models and observations at northern midlatitudes, Journal of Geophysical Research: Atmospheres, 119(9), 5719–5736, https://doi.org/10.1002/2013JD021435, 2014.

Pleim, J. E.: A Combined Local and Nonlocal Closure Model for the Atmospheric Boundary Layer. Part I: Model Description and Testing, Journal of Applied Meteorology and Climatology, 46(9), 1383–1395, https://doi.org/10.1175/JAM2539.1, 2007.

Pusede, S. E., Steiner, A. L. and Cohen, R. C.: Temperature and Recent Trends in the Chemistry of Continental Surface Ozone, Chem. Rev., 115(10), 3898–3918, https://doi.org/10.1021/cr5006815, 2015.

Rappenglück, B., Ackermann, L., Alvarez, S., Golovko, J., Buhr, M., Field, R. A., Soltis, J., Montague, D. C., Hauze, B., Adamson, S., Risch, D., Wilkerson, G., Bush, D., Stoeckenius, T., and Keslar, C.: Strong wintertime ozone events in the Upper Green River basin, Wyoming, 14, 4909–4934, https://doi.org/10.5194/acp-14-4909-2014, 2014.

Salma, I., Vörösmarty, M., Gyöngyösi, A. Z., Thén, W. and Weidinger, T.: What can we learn about urban air quality with regard to the first outbreak of the COVID-19 pandemic? A case study from central Europe, Atmospheric Chemistry and Physics, 20(24), 15725–15742, https://doi.org/10.5194/acp-20-15725-2020, 2020.

Seinfeld, J. H. and Pandis, S. N.: Atmospheric Chemistry and Physics: From Air Pollution to Climate Change, 2nd edition., Wiley-Interscience, Hoboken, N.J., 2006.

Shi, X. and Brasseur, G. P.: The Response in Air Quality to the Reduction of Chinese Economic Activities During the COVID-19 Outbreak, Geophysical Research Letters, 47(11), e2020GL088070, https://doi.org/10.1029/2020GL088070, 2020.

Sicard, P., De Marco, A., Agathokleous, E., Feng, Z., Xu, X., Paoletti, E., Rodriguez, J. J. D. and Calatayud, V.: Amplified ozone pollution in cities during the COVID-19 lockdown, Science of The Total Environment, 735, 139542, https://doi.org/10.1016/j.scitotenv.2020.139542, 2020.

Sillman, S.: The relation between ozone, NOx and hydrocarbons in urban and polluted rural environments, Atmospheric Environment, 33(12), 1821–1845, https://doi.org/10.1016/S1352-2310(98)00345-8, 1999.

Silvern, R. F., Jacob, D. J., Mickley, L. J., Sulprizio, M. P., Travis, K. R., Marais, E. A., Cohen, R. C., Laughner, J. L., Choi, S., Joiner, J. and Lamsal, L. N.: Using satellite observations of tropospheric NO_2 columns to infer long-term trends in US NO_x emissions: the importance of accounting for the free tropospheric NO_2 background, Atmospheric Chemistry and Physics, 19(13), 8863–8878, https://doi.org/10.5194/acp-19-8863-2019, 2019.

Skamarock, W. C. and Klemp, J. B.: A time-split nonhydrostatic atmospheric model for weather research and forecasting applications, Journal of Computational Physics, 227(7), 3465–3485, https://doi.org/10.1016/j.jcp.2007.01.037, 2008.

Souri, A. H., Nowlan, C. R., González Abad, G., Zhu, L., Blake, D. R., Fried, A., Weinheimer, A. J., Wisthaler, A., Woo, J.-H., Zhang, Q., Chan Miller, C. E., Liu, X. and Chance, K.: An inversion of NO_x and non-methane volatile organic compound (NMVOC) emissions using satellite observations during the KORUS-AQ campaign and implications for surface ozone over East Asia, Atmospheric Chemistry and Physics, 20(16), 9837–9854, https://doi.org/10.5194/acp-20-9837-2020, 2020a.

Souri, A. H., Nowlan, C. R., Wolfe, G. M., Lamsal, L. N., Chan Miller, C. E., Abad, G. G., Janz, S. J., Fried, A., Blake, D. R., Weinheimer, A. J., Diskin, G. S., Liu, X. and Chance, K.: Revisiting the effectiveness of HCHO/NO2 ratios for inferring ozone sensitivity to its precursors using high resolution airborne remote sensing observations in a high ozone episode during the KORUS-AQ campaign, Atmospheric Environment, 224, 117341, https://doi.org/10.1016/j.atmosenv.2020.117341, 2020b.

Souri, Amir H., Chance, K., Bak, J., Nowlan, C., González Abad, G., Jung, Y., Wong, D., Mao, J., Liu, X.: COVID-19-Europe-Ozone-NOx-VOC, Mendeley Data, V1, doi: 10.17632/jchfxsrvsb.1, 2021

Stavrakou, T., Müller, J.-F., Bauwens, M., De Smedt, I., Van Roozendael, M., Guenther, A., Wild, M. and Xia, X.: Isoprene emissions over Asia 1979–2012: impact of climate and land-use changes, Atmospheric Chemistry and Physics, 14(9), 4587–4605, https://doi.org/10.5194/acp-14-4587-2014, 2014.

Su, T., Li, Z. and Kahn, R.: Relationships between the planetary boundary layer height and surface pollutants derived from lidar observations over China: regional pattern and influencing factors, Atmospheric Chemistry and Physics, 18(21), 15921–15935, https://doi.org/10.5194/acp-18-15921-2018, 2018.

Thornton, J. A., Wooldridge, P. J., Cohen, R. C., Martinez, M., Harder, H., Brune, W. H., Williams, E. J., Roberts, J. M., Fehsenfeld, F. C., Hall, S. R., Shetter, R. E., Wert, B. P. and Fried, A.: Ozone production rates as a function of NOx abundances and HOx production rates in the Nashville urban plume, Journal of Geophysical Research: Atmospheres, 107(D12), ACH 7-1-ACH 7-17, https://doi.org/10.1029/2001JD000932, 2002.

United Nations Conference on Trade and Development Report, Accessed Dec 2020, https://unctad.org/system/files/official-document/dtltlbinf2020d1_en.pdf

Valin, L. C., Fiore, A. M., Chance, K. and Abad, G. G.: The role of OH production in interpreting the variability of CH2O columns in the southeast U.S., Journal of Geophysical Research: Atmospheres, 121(1), 478–493, https://doi.org/10.1002/2015JD024012, 2016.

Verhoelst, T., Compernolle, S., Pinardi, G., Lambert, J.-C., Eskes, H. J., Eichmann, K.-U., Fjæraa, A. M., Granville, J., Niemeijer, S., Cede, A., Tiefengraber, M., Hendrick, F., Pazmiño, A., Bais, A., Bazureau, A., Boersma, K. F., Bognar, K., Dehn, A., Donner, S., Elokhov, A., Gebetsberger, M., Goutail, F., Grutter de la Mora, M., Gruzdev, A., Gratsea, M., Hansen, G. H., Irie, H., Jepsen, N., Kanaya, Y., Karagkiozidis, D., Kivi, R., Kreher, K., Levelt, P. F., Liu, C., Müller, M., Navarro Comas, M., Piters, A. J. M., Pommereau, J.-P., Portafaix, T., Prados-Roman, C., Puentedura, O., Querel, R., Remmers, J., Richter, A., Rimmer, J., Rivera Cárdenas, C., Saavedra de Miguel, L., Sinyakov, V. P., Stremme, W., Strong, K., Van Roozendael, M., Veefkind, J. P., Wagner, T., Wittrock, F., Yela González, M. and Zehner, C.: Ground-based validation of the Copernicus Sentinel-5P TROPOMI NO2 measurements with the NDACC ZSL-DOAS, MAX-DOAS and Pandonia global networks, Atmospheric Measurement Techniques, 14(1), 481–510, https://doi.org/10.5194/amt-14-481-2021, 2021.

Vigouroux, C., Langerock, B., Bauer Aquino, C. A., Blumenstock, T., Cheng, Z., De Mazière, M., De Smedt, I., Grutter, M., Hannigan, J. W., Jones, N., Kivi, R., Loyola, D., Lutsch, E., Mahieu, E., Makarova, M., Metzger, J.-M., Morino, I., Murata, I., Nagahama, T., Notholt, J., Ortega, I., Palm, M., Pinardi, G., Röhling, A., Smale, D., Stremme, W., Strong, K., Sussmann, R., Té, Y., van Roozendael, M., Wang, P. and Winkler, H.: TROPOMI–Sentinel-5 Precursor formaldehyde validation using an extensive network of ground-based Fourier-transform infrared stations, Atmospheric Measurement Techniques, 13(7), 3751–3767, https://doi.org/10.5194/amt-13-3751-2020, 2020.

Wang, P., Piters, A., van Geffen, J., Tuinder, O., Stammes, P. and Kinne, S.: Shipborne MAX-DOAS measurements for validation of TROPOMI NO_2 products, Atmospheric

Measurement Techniques, 13(3), 1413–1426, https://doi.org/10.5194/amt-13-1413-2020, 2020.

Wang, W., Parrish, D. D., Li, X., Shao, M., Liu, Y., Mo, Z., Lu, S., Hu, M., Fang, X., Wu, Y., Zeng, L. and Zhang, Y.: Exploring the drivers of the increased ozone production in Beijing in summertime during 2005–2016, Atmospheric Chemistry and Physics, 20(24), 15617–15633, https://doi.org/10.5194/acp-20-15617-2020, 2020.

Wolfe, G. M., Kaiser, J., Hanisco, T. F., Keutsch, F. N., de Gouw, J. A., Gilman, J. B., Graus, M., Hatch, C. D., Holloway, J., Horowitz, L. W., Lee, B. H., Lerner, B. M., Lopez-Hilifiker, F., Mao, J., Marvin, M. R., Peischl, J., Pollack, I. B., Roberts, J. M., Ryerson, T. B., Thornton, J. A., Veres, P. R. and Warneke, C.: Formaldehyde production from isoprene oxidation across NO_x regimes, Atmospheric Chemistry and Physics, 16(4), 2597–2610, https://doi.org/10.5194/acp-16-2597-2016, 2016.

Wyche, K. P., Nichols, M., Parfitt, H., Beckett, P., Gregg, D. J., Smallbone, K. L. and Monks, P. S.: Changes in ambient air quality and atmospheric composition and reactivity in the South East of the UK as a result of the COVID-19 lockdown, Science of The Total Environment, 755, 142526, https://doi.org/10.1016/j.scitotenv.2020.142526, 2021.

Xiu, A. and Pleim, J. E.: Development of a Land Surface Model. Part I: Application in a Mesoscale Meteorological Model, Journal of Applied Meteorology and Climatology, 40(2), 192–209, https://doi.org/10.1175/1520-0450(2001)040<0192:DOALSM>2.0.CO;2, 2001.

Yienger, J. J. and Levy, H.: Empirical model of global soil-biogenic NOx emissions, Journal of Geophysical Research, 100(D6), 11447–11464, https://doi.org/10.1029/95JD00370, 1995.

Zhao, X., Griffin, D., Fioletov, V., McLinden, C., Cede, A., Tiefengraber, M., Müller, M., Bognar, K., Strong, K., Boersma, F., Eskes, H., Davies, J., Ogyu, A. and Lee, S. C.: Assessment of the quality of TROPOMI high-spatial-resolution NO_2 data products in the Greater Toronto Area, Atmospheric Measurement Techniques, 13(4), 2131–2159, https://doi.org/10.5194/amt-13-2131-2020, 2020.

Table 1. Statistics reported in several validations studies comparing TROPOMI tropospheric NO_2 against independent observations.

Study	Location	Time Period	Benchmark Instrument	Bias (low)	Dispersion	Modification	Modified Bias (low)
Chan et al. 2020	Munich	May 2018-Apr 2019	MAX-DOAS	30%	N/A	In-situ MAX-DOAS profiles	17%
Griffin et al. 2019	Canadian Oil Sands	Mar-May 2018 (v1.01)	Pandora (direct Sun)	15-30%	N/A	Higher resolution profiles (10 km) and albedo	0-25%
Judd et al. 2020	New York	Jun-Sep 2018	GeoTASO	19-33%	N/A	Higher resolution profiles (12 km)	7-19%
Verhoelst et al. 2020	Global	Apr 2018-Feb 2020	MAX-DOAS	37% (average), 23-51% (range)	3.5×10^{15} molec/cm^2	N/A	N/A
Wang P. et al. 2020	Atlantic and Pacific Oceans	4 campaigns during Dec 2018-Jul 2019	MAX-DOAS	Negligible	N/A	N/A	N/A
Zhao et al. 2020	Greater Toronto Area	Mar 2018-Mar 2019	Pandora (direct Sun)	24-28% (suburban/urban) +4-10% (rural)		Higher resolution profiles (10 km) and albedo	13-24% (suburban/urban) +14-15% (rural)

Table 2. Relative and absolute differences of top-down estimate of NO_x emissions using TROPOMI for different countries in Europe in 2020 (lockdown) with respect to 2019 (baseline). Relative numbers are calculated with respect to values in 2019. Ton and d denote tonne and day, respectively.

Countries	**March (%, ton/d)**		**April (%, ton/d)**		**May (%, ton/d)**	
Austria	-17.2	-63.4	-6.6	-23.3	-3.8	-12.2
Belarus	-13.0	-67.9	-15.4	-88.9	-4.2	-19.2
Belgium	-32.6	-159.3	-27.3	-137.9	-28.6	-177.6
Czech Republic	-23.7	-113.3	-9.7	-43.5	-2.8	-11.3
Denmark	-10.9	-17.9	-13.1	-29.6	-8.1	-19.8
Finland	-2.9	-5.9	-7.7	-18.2	-8.8	-19.4
France	-25.3	-547.2	-20.5	-467.4	-9.3	-198.2
Germany	-7.2	-203.6	-24.4	-832.9	-9.6	-285.6
Greece	-20.6	-77.9	-5.3	-19.9	-0.9	-3.4
Hungary	-12.2	-34.1	-6.2	-18.6	-5.0	-12.2
Ireland	-12.5	-24.5	-7.5	-16.8	-3.7	-8.1
Italy	-17.8	-270.6	-16.1	-252.2	+2.4	+34.1
Netherlands	+8.9	+28.3	-9.7	-39.0	-2.3	-11.0
Norway	-2.9	-7.7	-8.9	-26.9	-3.4	-9.5
Poland	-15.0	-246.1	-20.0	-342.9	-8.3	-126.7
Portugal	-8.8	-24.4	-8.8	-23.3	-3.4	-10.2
Romania	-12.9	-70.8	-1.1	-5.8	+1.1	+5.2
Spain	-10.1	-156.2	-12.5	-192.2	-2.1	-32.4
Sweden	-6.6	-15.2	-8.9	-23.1	-6.4	-15.8
Switzerland	-8.5	-14.1	-8.0	-13.2	-13.0	-19.0
Turkey	-10.5	-224.3	-4.0	-76.6	-5.2	-98.7
Ukraine	-13.6	-224.2	-12.3	-198.0	-13.8	-207.1
United Kingdom	-14.9	-254.8	-19.1	-334.3	-14.3	-263.9
The strait of Gibraltar and Alboran Sea	-7.2	-77.3	-8.6	-86.7	-14.3	-10.7
All	**-13.9 ± 8.4**	**-2795.6± 129.7**	**-15.4 ± 6.7**	**-3224.6 ± 194.5**	**-7.7 ± 6.5**	**-1522.45 ± 92.0**

Table 3. Reaction rates relating to the chemical pathways of ozone formation and loss over box L (proximity of central Europe).

Reactions	**Production (P) or loss (L)**	**April 2020 (ppbv/hr)**	**April 2019 (ppbv/hr)**	**Net diff [a](ppbv/hr)**
HO_2+NO	P	0.85	0.91	-0.06
RO_2+NO	P	0.44	0.41	+0.03
NO_2+OH	L	0.10	0.14	+0.04
O^1D+H_2O	L	0.07	0.08	+0.01
O_3+VOCs	L	0.01	0.01	0.00
O_3+HO_x	L	0.09	0.08	-0.01
$J_{NO2}[NO_2]$	P	14.61	27.28	-12.67
$k_{NO+O3}[NO][O_3]$	L	15.11	28.52	+13.40
$J_{NO2}[NO_2]- k_{NO+O3}[NO][O_3]$	N/A	-0.50	-1.24	+0.74
Numerically solved PO_3	N/A	-0.79	-1.53	+0.74

[a] A positive net difference indicates higher (lower) production (loss) in 2020 with respect to 2019.

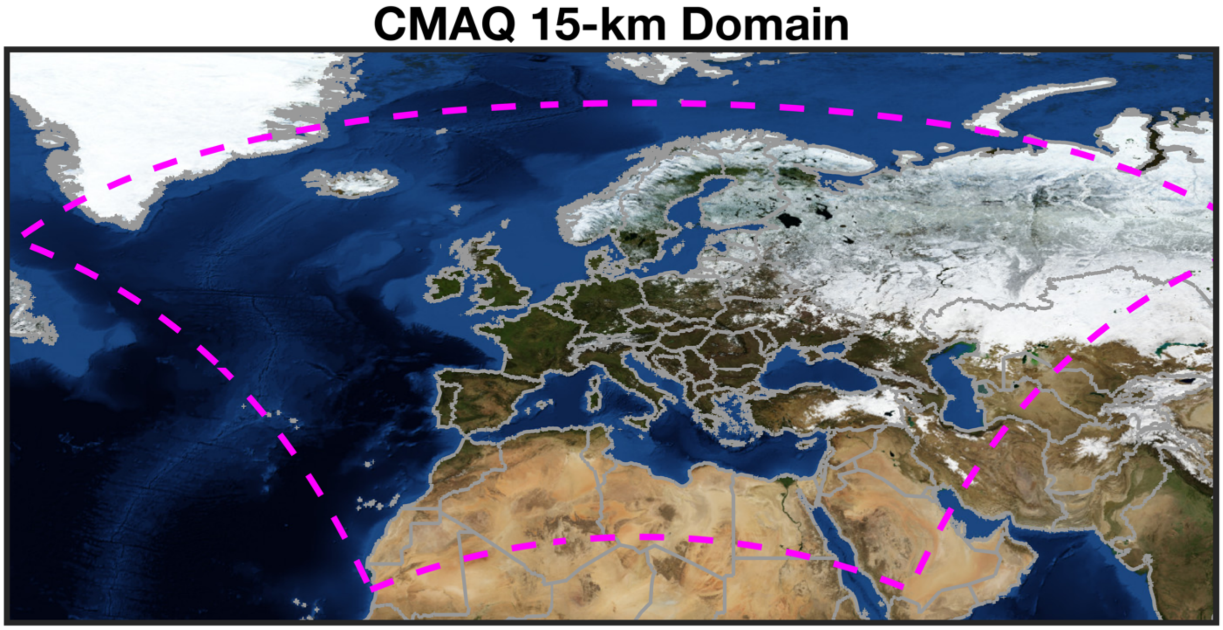

Figure 1. The WRF-CMAQ 15 km domain covering Europe. The background picture is based on the publicly available NASA Blue Marble (© NASA).

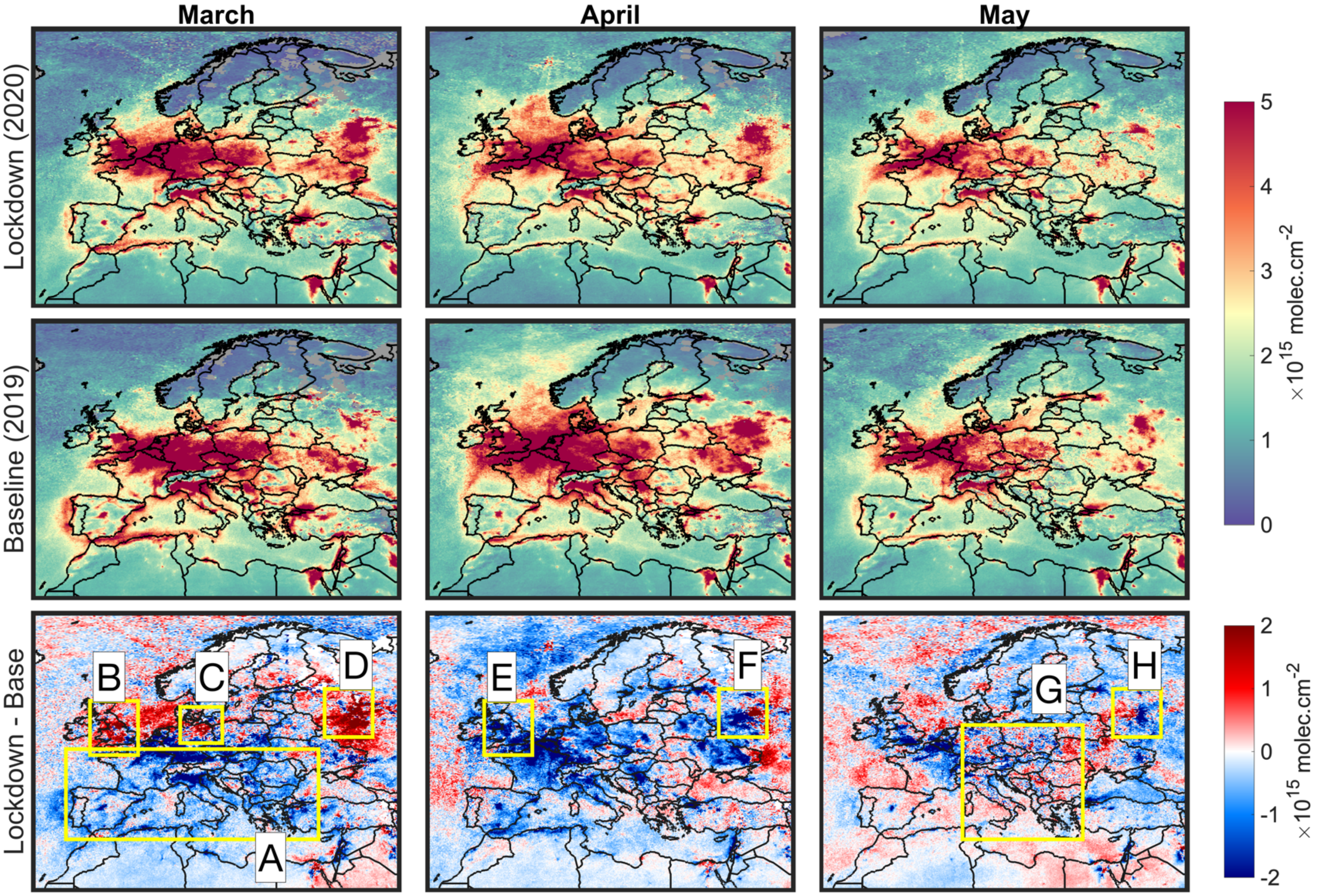

Figure 2. (first row) Maps of tropospheric NO_2 from the TROPOMI sensor during months of March, April, and May in 2020 (lockdown). (second row) Same as the first row but for the baseline year (2019). (last row), Difference of the columns in 2020 with respect to those of 2019. All columns are corrected for the bias and their AMFs are recalculated iteratively based on the posterior profiles derived from our inverse modeling practice. The satellite-derived columns are subject to errors, so a direct interpretation of their magnitudes cannot be performed in a robust manner.

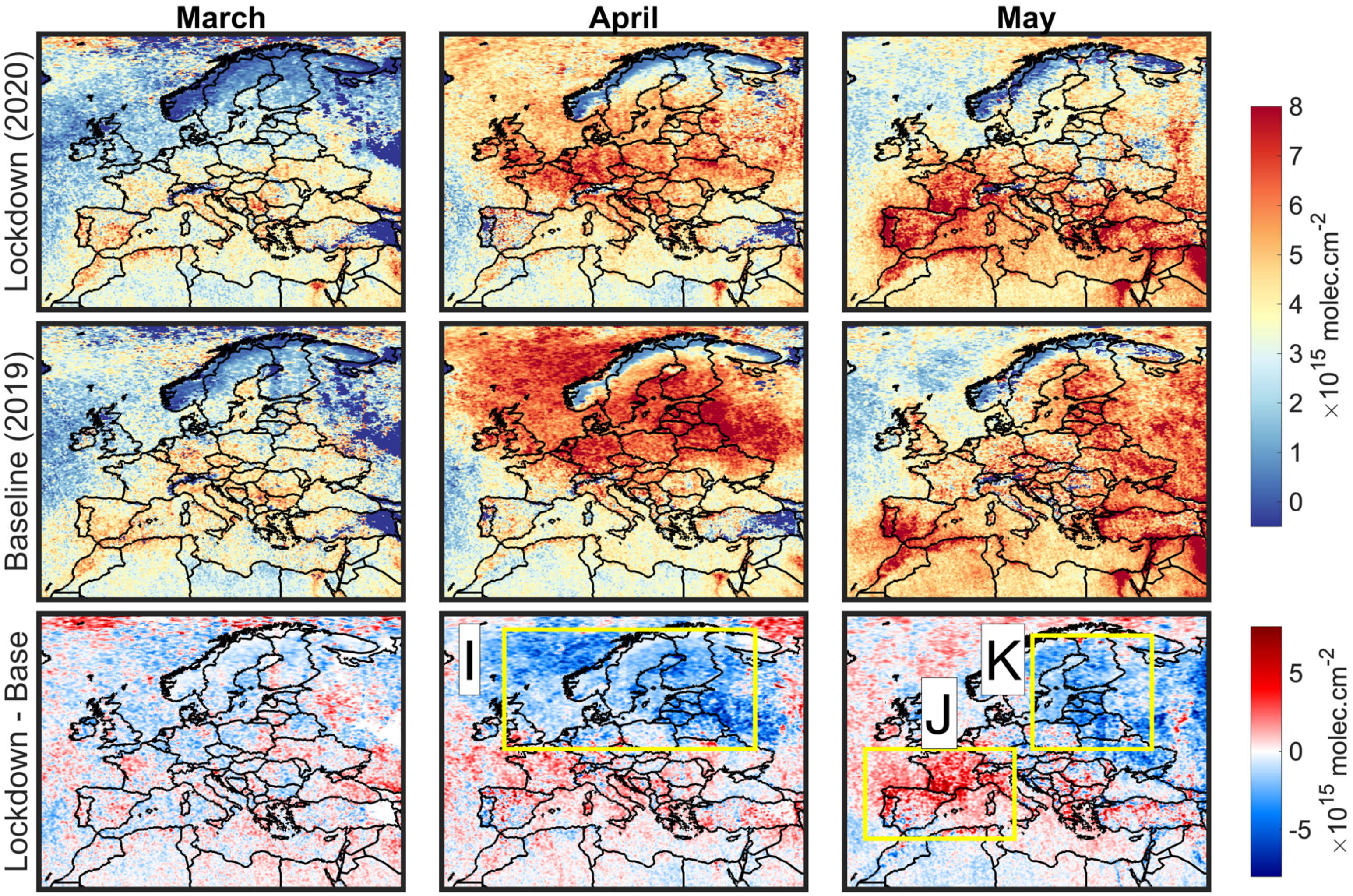

Figure 3. Same as Figure 2 but for the total HCHO columns.

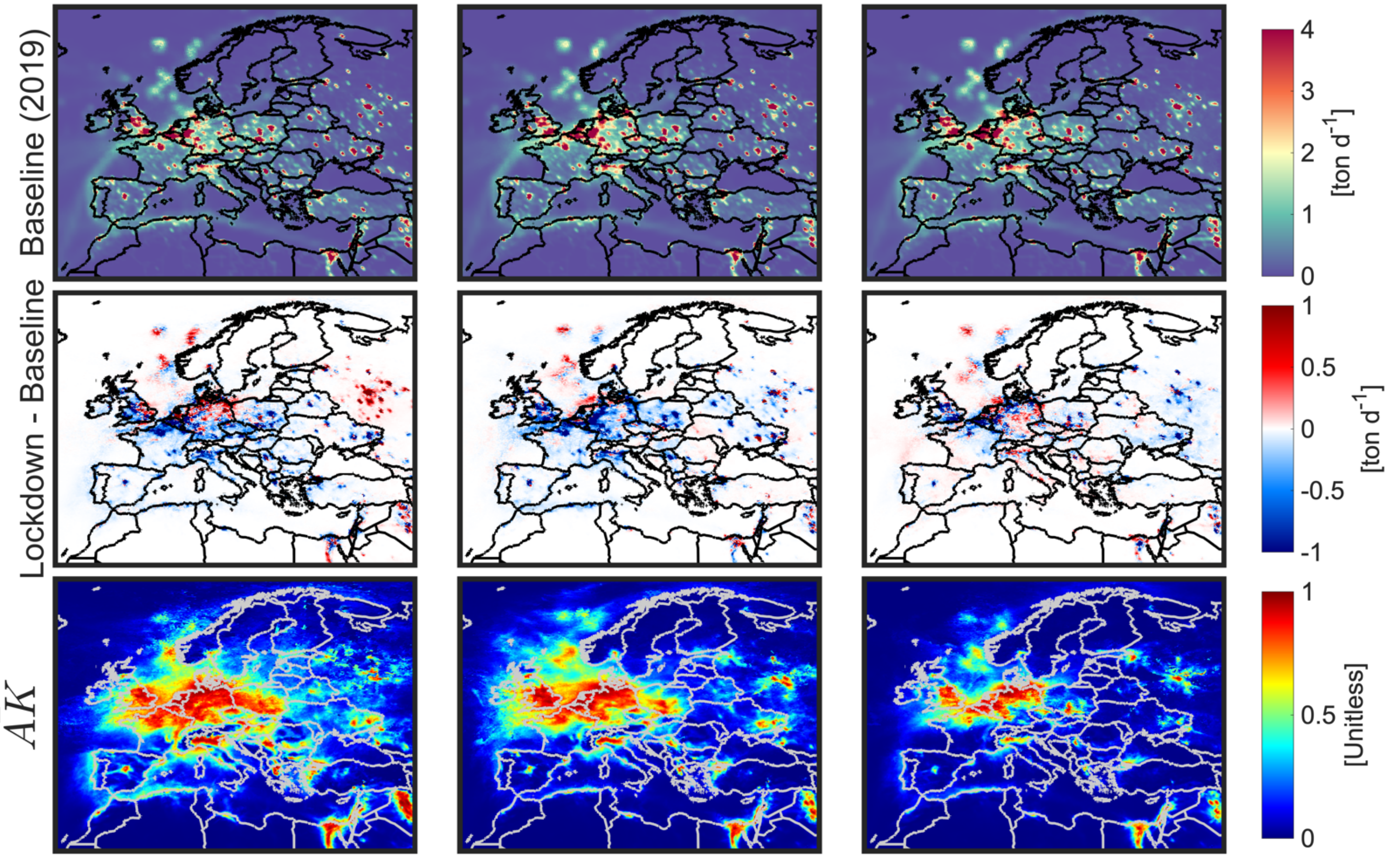

Figure 4. Top-down estimates of total NO_x during months of March, April and May in 2019 (baseline) and the differences between emission in 2020 (lockdown) and 2019. To infer the magnitude of emissions in 2020, the second row should be added to the first one. Both TROPOMI HCHO and NO_2 observations are jointly used to estimate these numbers. Averaging kernels (mean values based on both 2019 and 2020 estimates) describe the level of credibility of the estimate which is heavily dependent on the TROPOMI signal-to-noise ratios.

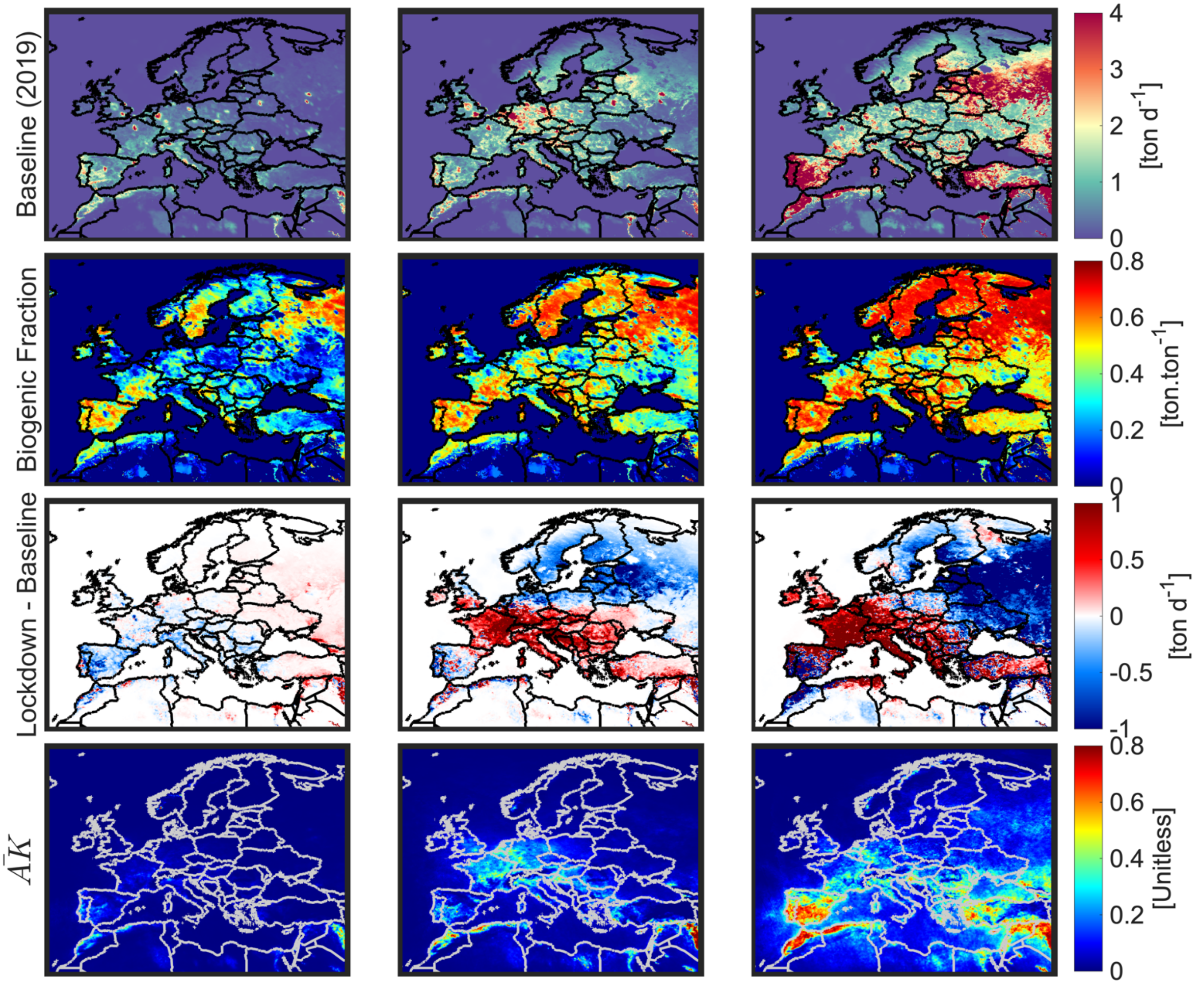

Figure 5. Same as Figure 4 but for the total VOC emissions. Biogenic fractions are based on the average values in 2019 and 2020.

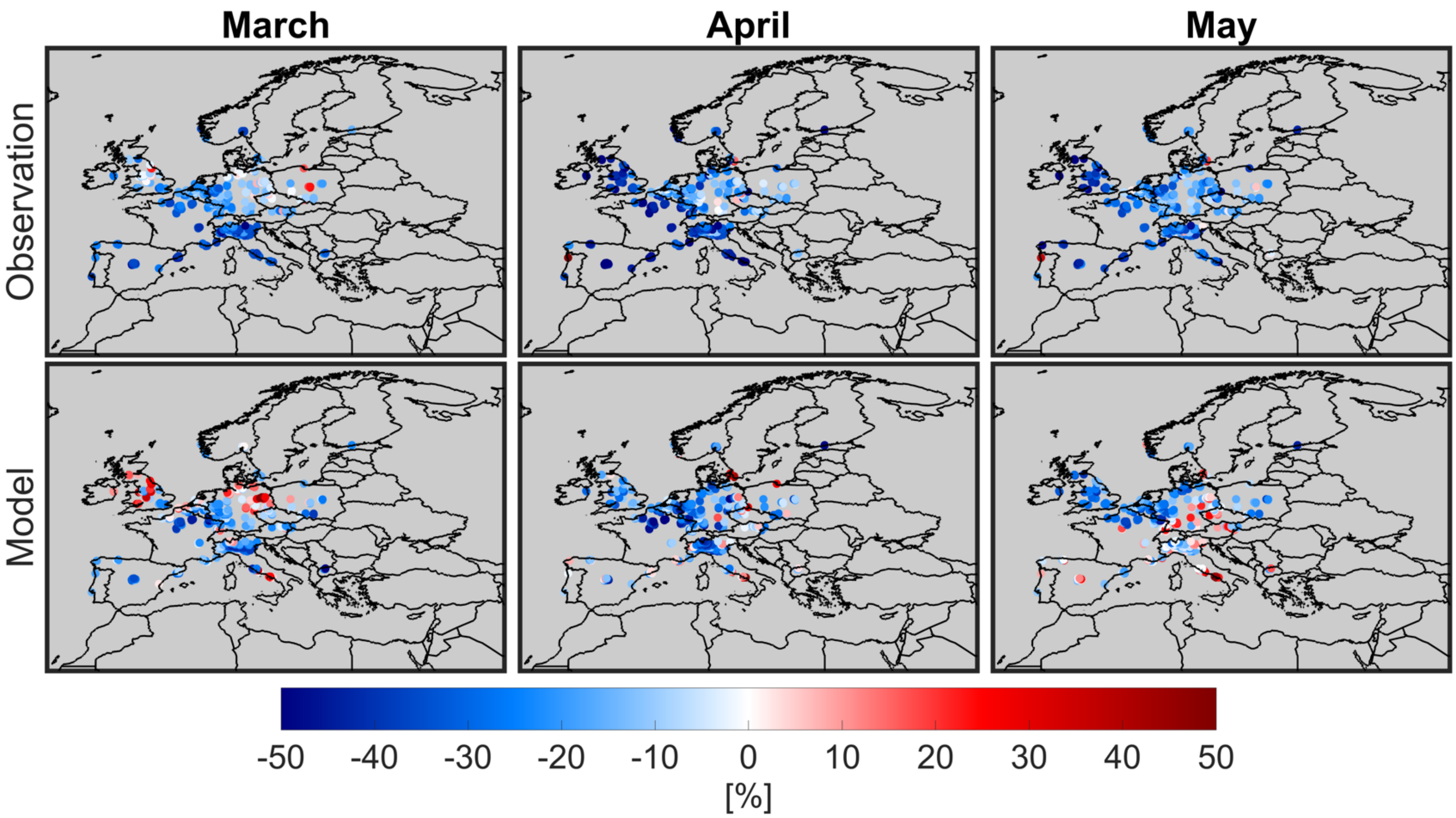

Figure 6. Scatter maps of relative changes in surface NO_2 concentrations suggested by the European air quality network (first row), and the constrained model (second row). Results are daily-averaged. We only consider grid cells whose averaging kernels (from the NO_x inversion) are above 0.5. Furthermore, grid cells having more than 2 stations are only included to partly account for the spatial representivity factor. Surface concentrations are not accounted for the NO_z family interferences.

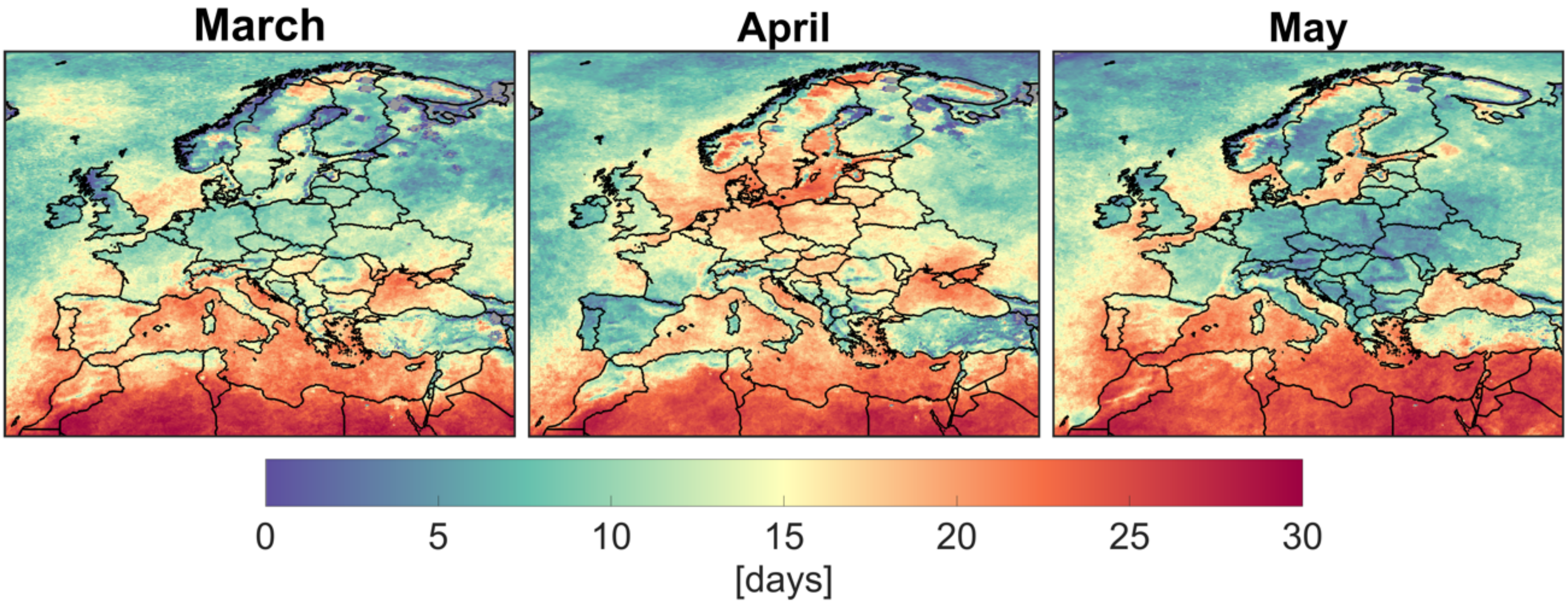

Figure 7. The average number of good quality (qa_flag>0.75) TROPOMI tropospheric NO_2 days observed at 15×15 km^2 in 2019 and 2020. These numbers are heavily affected by cloudiness.

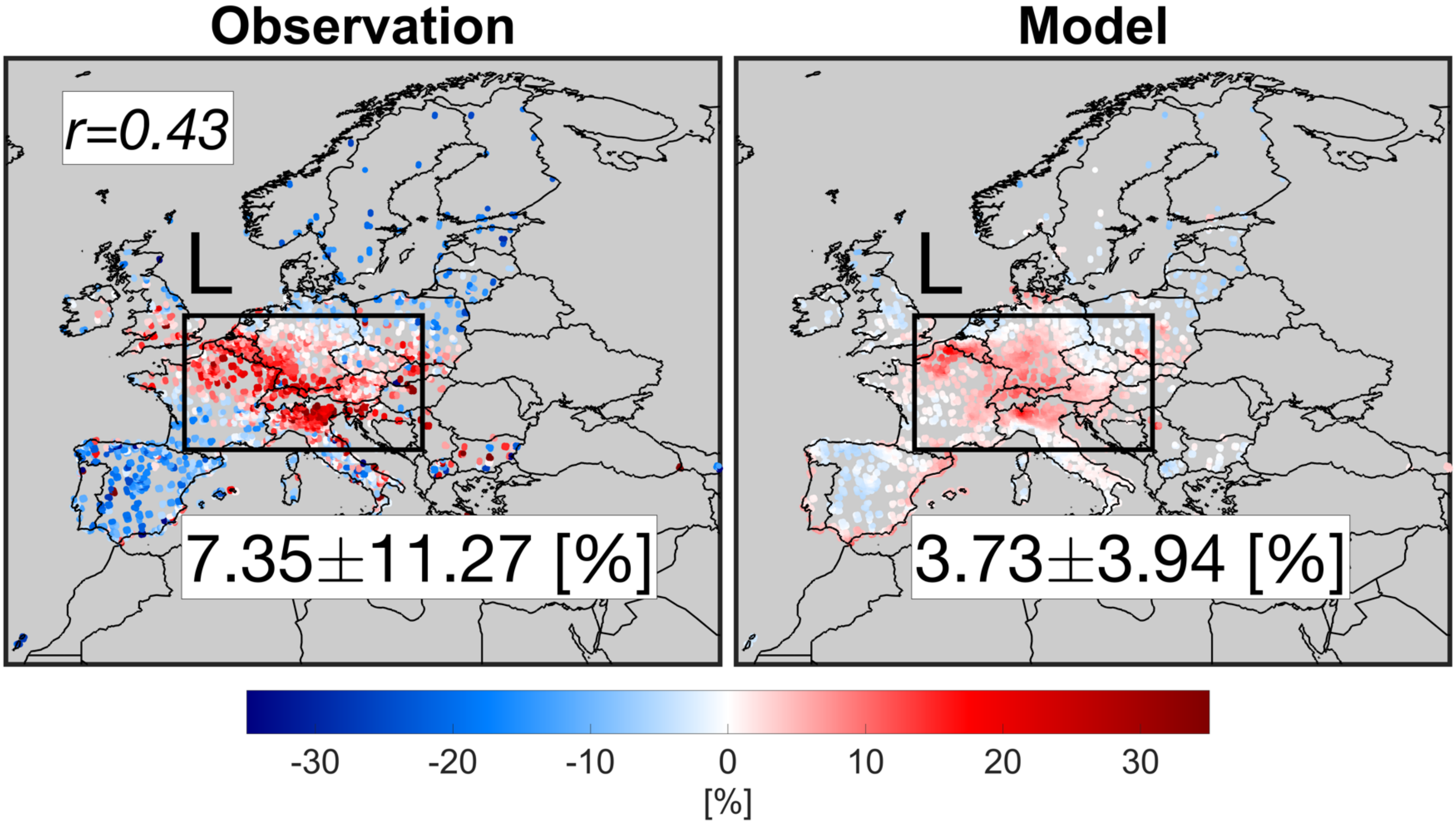

Figure 8. Changes in surface MDA8 ozone concentrations suggested by the observation (left), and the constrained model (right) in April 2020 relative to those in 2019.

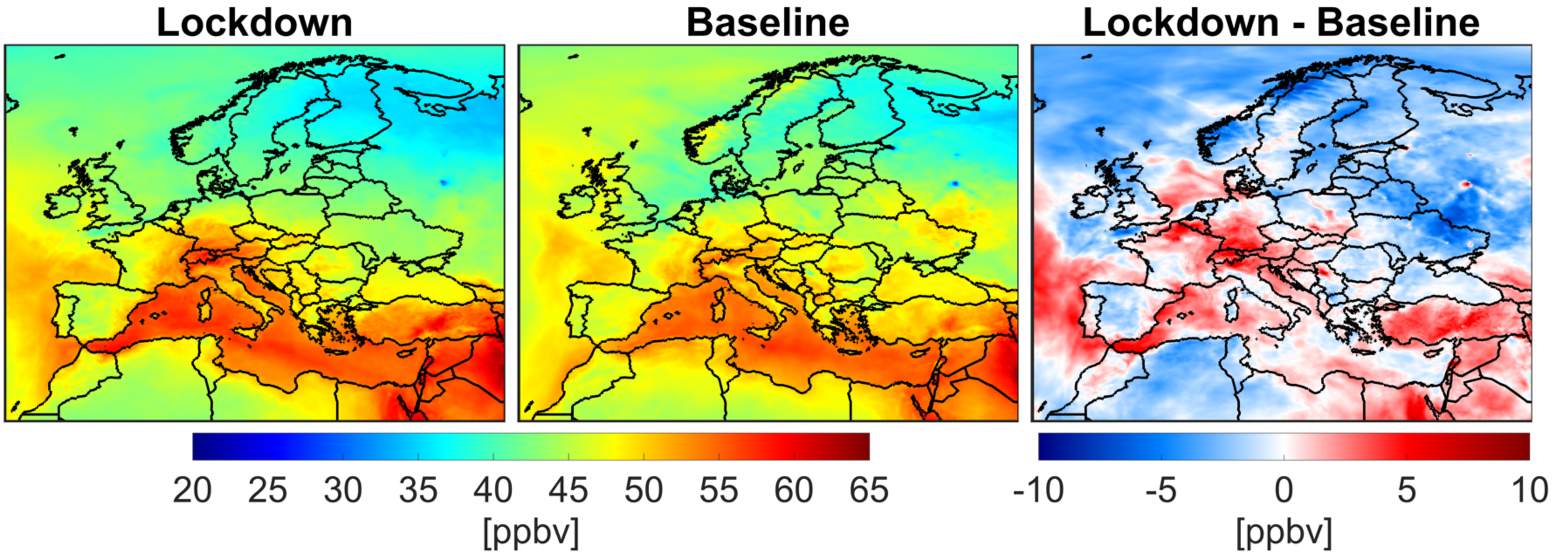

Figure 9. Simulated surface MDA8 ozone concentration using the constrained model in the month of April 2020 (lockdown), April 2019 (baseline), and their difference.

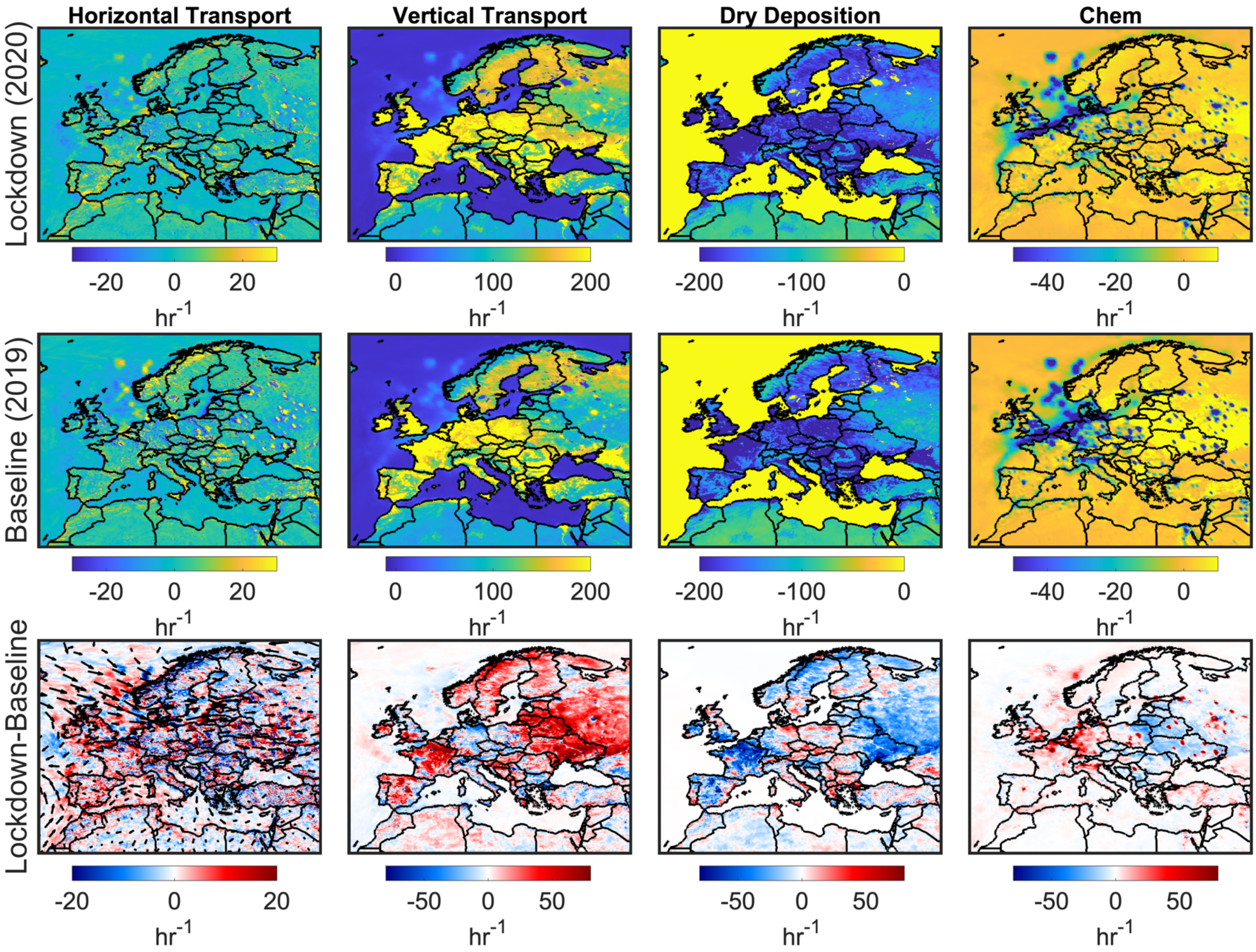

Figure 10. Surface process tendencies (hr^{-1}) including horizontal transport (advection plus diffusion), vertical transport (advection plus diffusion), dry deposition, and chemistry. Positive (negative) values mean source (sink) of ozone. These outputs are based on the constrained model. Wind vectors are the difference.

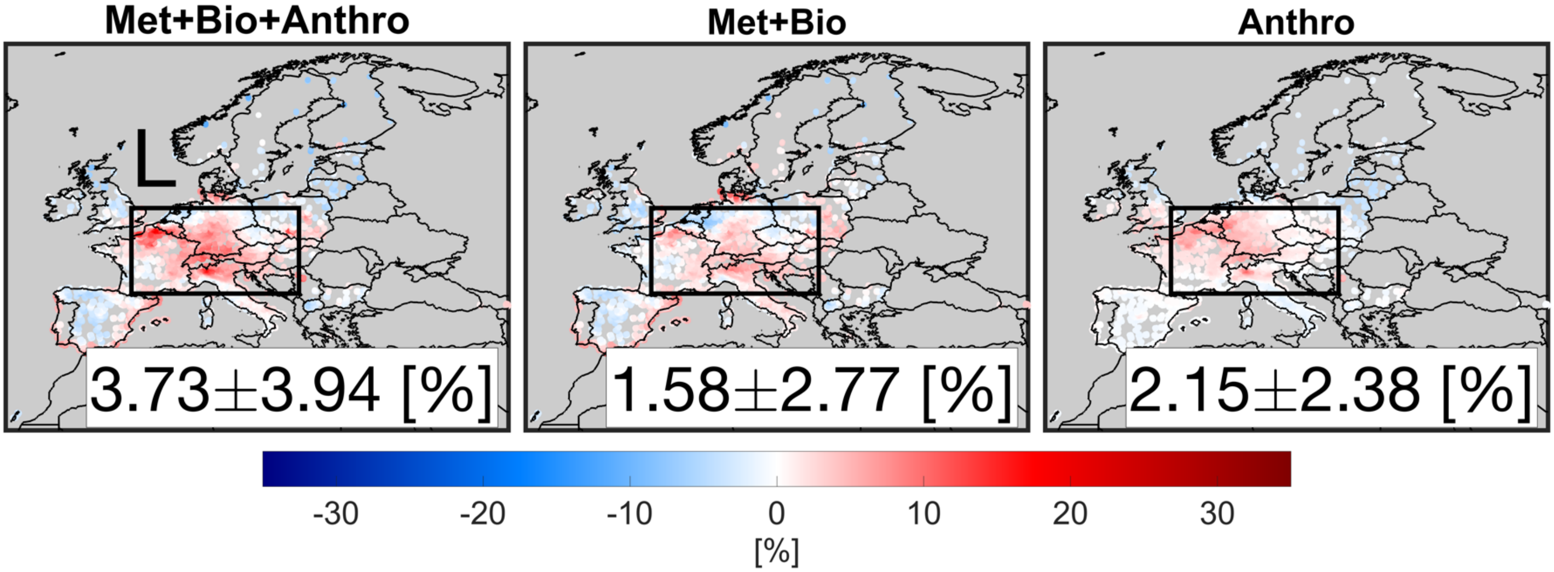

Figure 11. Simulated MDA8 surface ozone difference between April 2020 with respect to April 2019 including (left) dynamical meteorology, biogenic and anthropogenic emissions, (middle) dynamical meteorology and biogenic emissions, and (right) the subtraction of the previous scenarios isolating dynamical anthropogenic emissions. Emissions used for these experiments are based on the top-down estimates.

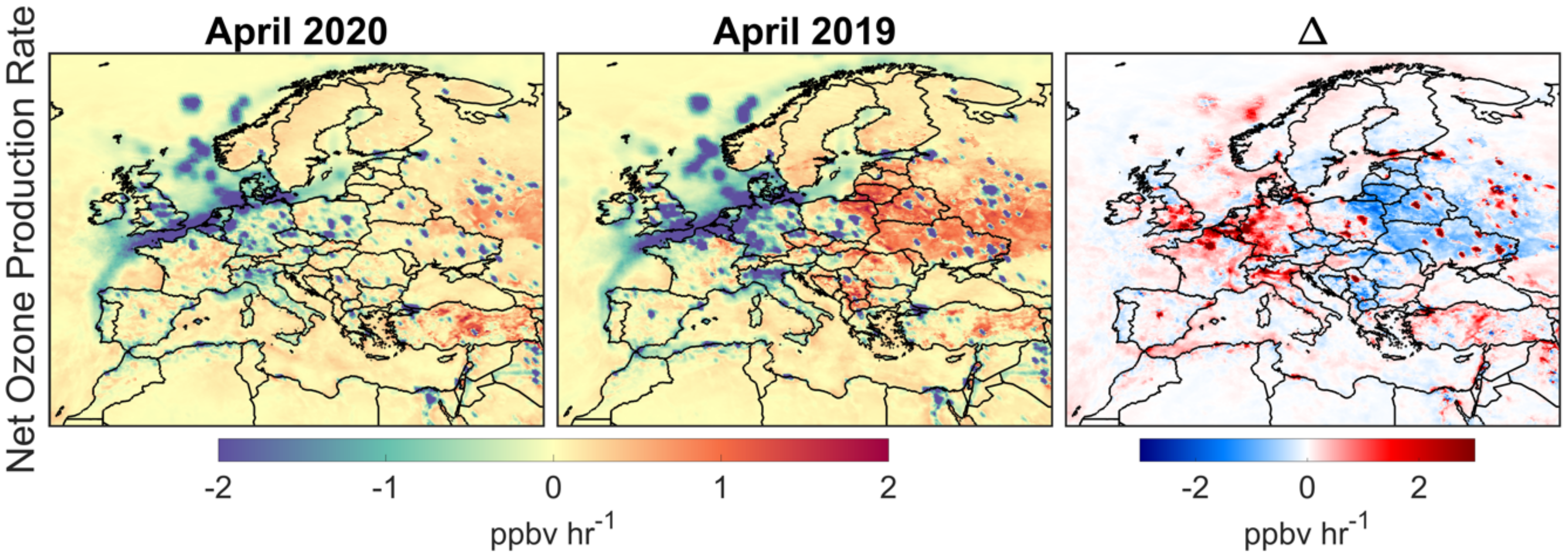

Figure 12. Numerically-solved net ozone production rates based on the WRF-CMAQ simulations using the constrained emissions by the satellite data in April 2020, 2019, and the difference. These values are over the surface and are averaged during the MDA8 hours.

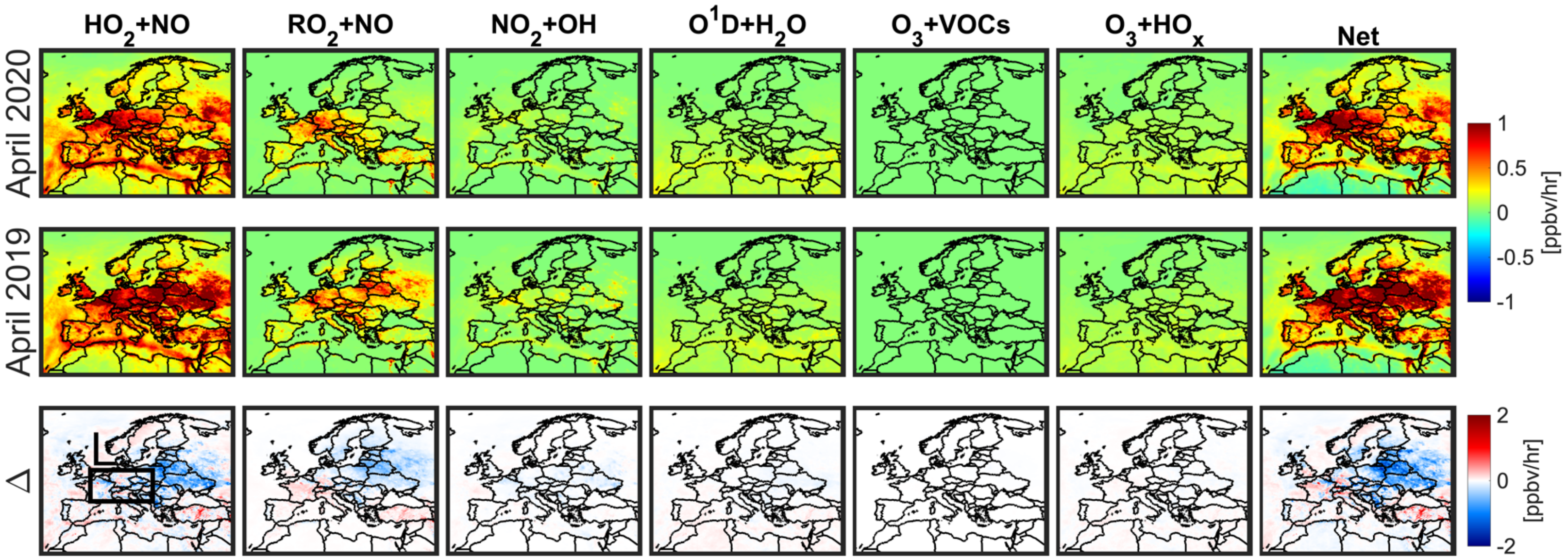

Figure 13. Surface chemical processes involved in equation 5 (ppbv hr^{-1}) pertaining to the production and loss of ozone in April 2020 (lockdown) and 2019 (baseline) during MDA8 hours. These outputs are based on the constrained model.

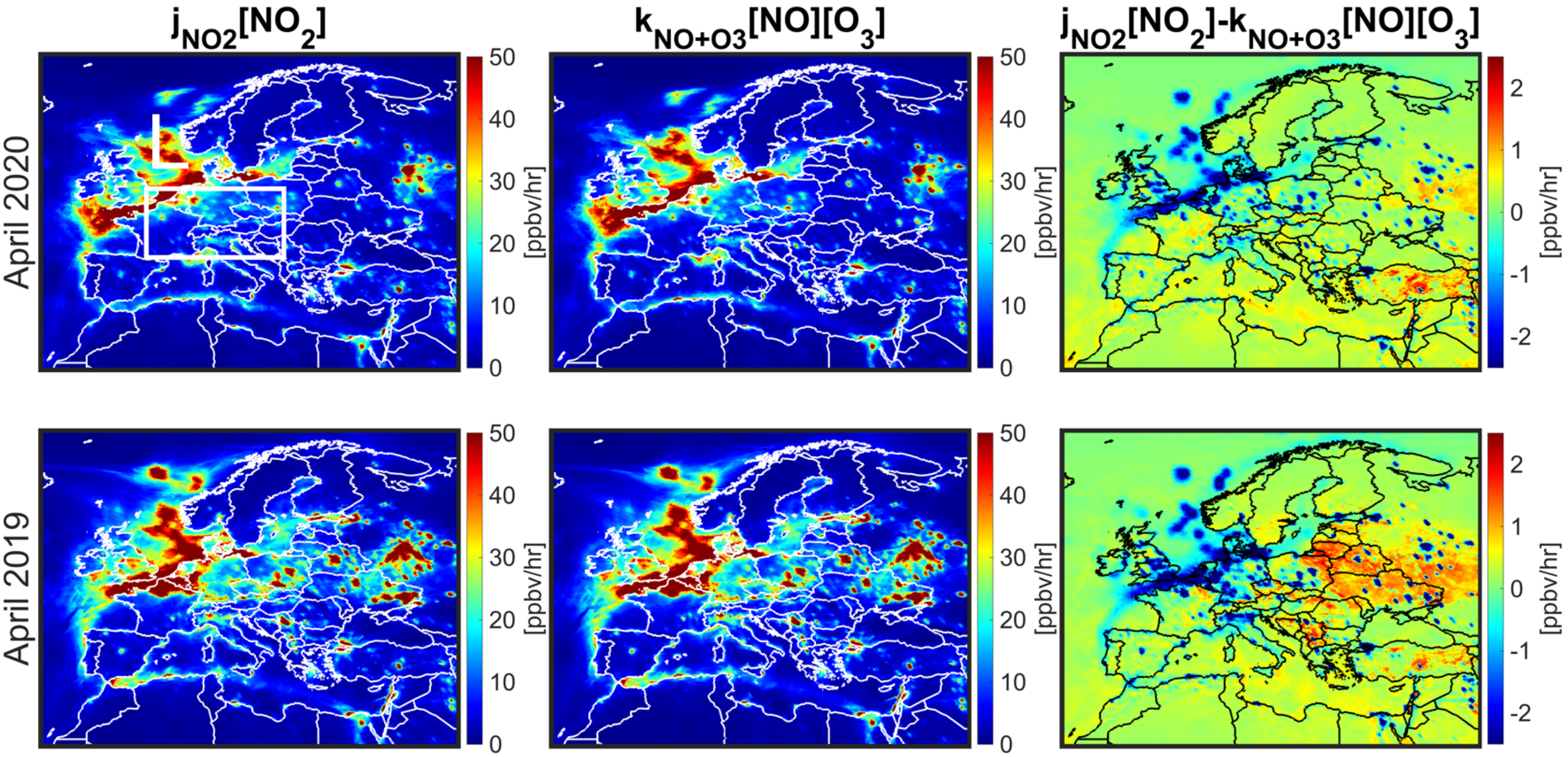

Figure 14. Surface chemical processes involved in equation 6 (ppbv hr^{-1}) pertaining to the O_3-NO-NO_2 partitioning in April 2020 and 2019 during MDA8 hours. The constrained model by the satellite observations are used to derive these outputs.